

DOI: 10.1002/ ((please add manuscript number))

Article type: **Full Paper**

Enhancing charge carrier lifetime in metal oxide photoelectrodes through mild

hydrogen treatment

*Ji-Wook Jang, Dennis Friedrich, Sönke Müller, Marlene Lamers, Hannes Hempel, Sheikha Lardhi, Zhen Cao, Moussab Harb, Luigi Cavallo, René Heller, Rainer Eichberger, Roel van de Krol, and Fatwa F. Abdi**

Dr. J.-W. Jang, Dr. D. Friedrich, S. Müller, M. Lamers, Dr. R. Eichberger, Prof. R. van de Krol, Dr. F. F. Abdi

Institute for Solar Fuels, Helmholtz-Zentrum Berlin für Materialien und Energie GmbH, Hahn-Meitner-Platz 1, Berlin 14109, Germany

E-mail: fatwa.abdi@helmholtz-berlin.de

H. Hempel

Department of Structure and Dynamics of Energy Materials, Helmholtz-Zentrum Berlin für Materialien und Energie GmbH, Hahn-Meitner-Platz 1, Berlin 14109, Germany

S. Lardhi, Dr. Z. Cao, Dr. M. Harb, Prof. L. Cavallo

King Abdullah University of Science and Technology (KAUST), KAUST Catalysis Center (KCC), Physical Sciences and Engineering Division (PSE), Thuwal, 23955-6900, Saudi Arabia

Dr. R. Heller

Institute of Ion Beam Physics and Materials Research, Helmholtz-Zentrum Dresden-Rossendorf, Dresden 01328, Germany

Keywords: solar water splitting, BiVO₄, time-resolved spectroscopy, hydrogen treatment, carrier lifetime

Abstract: Widespread application of solar water splitting for energy conversion is largely dependent on the progress in developing not only efficient, but also cheap and scalable photoelectrodes. Metal oxides, which can be deposited with scalable techniques and are relatively cheap, are particularly interesting, but high efficiency is still hindered by the poor carrier transport properties (i.e., carrier mobility and lifetime). In this paper, a mild hydrogen treatment is introduced to bismuth vanadate (BiVO_4), which is one of the most promising metal oxide photoelectrodes, as a method to overcome the carrier transport limitations. Time-resolved microwave and terahertz conductivity measurements reveal more than two-fold enhancement of the carrier lifetime for the hydrogen-treated BiVO_4 , without significantly affecting the carrier mobility. This is in contrast to the case of tungsten-doped BiVO_4 , although hydrogen is also shown to be a donor type dopant in BiVO_4 . The enhancement in carrier lifetime is found to be caused by significant reduction of trap-assisted recombination, either via passivation of deep trap states or reduction of trap state density, which can be related to vanadium anti-site on bismuth or vanadium interstitials according to density functional theory calculations. Overall, these findings provide further insights on the interplay between defect modulation and carrier transport in metal oxide photoelectrodes, which will benefit the development of low-cost, highly-efficient solar energy conversion devices.

1. Introduction

Rapid increase of the world energy consumption represents one of the biggest challenges that humanity faces in the 21st century. Experts have estimated that we will need ~30 TW in 2050, and 46 TW by the end of the century.^[1, 2] This large amount of energy cannot be provided by fossil fuels, since their supply is limited and their combustion produces large amounts of carbon dioxide (CO_2), which causes serious environmental consequences (e.g., global

warming). Recently, hydrogen received particular attention as an alternative fuel due to its high gravimetric energy density (142 MJ kg^{-1} vs. $< 1 \text{ MJ kg}^{-1}$ for batteries). In addition, it is fully renewable and no CO_2 is released when the hydrogen is used to drive a fuel cell. While this is encouraging, $\sim 95\%$ of the current hydrogen production is done via steam reforming of natural gas,^[3, 4] which releases CO_2 as the main by-product. In order to produce hydrogen in a completely clean and renewable fashion, sustainable energy sources, such as solar energy, need to be utilized for hydrogen production.

Photoelectrochemical (PEC) water splitting is one of the promising methods for producing hydrogen using sunlight.^[5, 6] Despite its promise, the commercialization of PEC water splitting is still far away due to the trade-off between efficiency, cost, and stability. High efficiencies, approaching 20%, have been shown by photoelectrodes based on high-quality III-V semiconductors (e.g., GaAs, GaInP₂, etc.).^[7-9] However, the cost of these photoelectrodes is likely to be prohibitive, and most of them suffer from instability in aqueous solutions. In contrast, metal oxide semiconductors are relatively cheap and stable in aqueous solutions, but photoelectrodes based on metal oxides have only shown moderate efficiencies ($< 8\%$).^[10-13] A major limitation of complex metal oxides is their poor charge carrier (electron and/or hole) transport properties. As an illustration, carrier mobilities can be as high as 8,500 and $1,500 \text{ cm}^2\text{V}^{-1}\text{s}^{-1}$ in GaAs and Si, respectively,^[14] while values of $\sim 0.01\text{-}0.1 \text{ cm}^2\text{V}^{-1}\text{s}^{-1}$ are observed for typical metal oxide photoelectrode materials, such as BiVO_4 and Fe_2O_3 .^[15-17] In addition, carrier lifetimes are usually short, in the order of pico- to nano-seconds.^[17-19] These low mobilities and short carrier lifetimes can be attributed to two factors inherent to metal oxides. First, many of the reported metal oxides are prepared through synthesis methods that tend to produce significant amounts of point defects. While certain defects may be desirable in order to enhance the n- or p-type conductivity of the material, others have energy levels deeper in the bandgap and may act as recombination centers, thus negatively affecting the carrier lifetimes. Second, carriers in metal oxides tend to be localized and form small

polarons.^[15, 20-22] Due to the ionic nature of metal oxides, carriers may become self-trapped in a potential well they create by polarizing the surrounding atoms. Additional energy in the form of phonons is needed for the surrounding atoms to alter their positions and allow carrier transport. In order to improve the carrier transport in metal oxides, we therefore need to develop methods to passivate the point defects that are performance-killers and/or modify the degree of carrier localization. A successful method will potentially break the efficiency-cost trade-off and lead to highly efficient, low cost photoelectrodes.

One of the methods that have been used to improve the PEC performance of metal oxides is hydrogen treatment. This simple post-synthesis annealing treatment under H₂ atmosphere has received considerable attention since Chen et al. reported hydrogenated black TiO₂ in 2011.^[23] It is also found to dramatically improve the PEC water splitting performance of other metal oxides, including the currently highest performing metal oxide photoanode, BiVO₄.^[24-28] The improved performance was initially assumed to originate from the increased electrical conductivity due to oxygen vacancy formation and/or hydrogen insertion (i.e., an increase in carrier density through donor doping).^[23-29] However, to the best of our knowledge, no report has yet provided direct evidence for the influence of hydrogen treatment on the carrier transport properties of BiVO₄.

In this paper, we show for the first time that hydrogen treatment increases the carrier lifetime in BiVO₄, and consequently the diffusion length, as directly measured by time-resolved microwave conductivity (TRMC). This observation is directly linked to the improved PEC performance (onset potential and photocurrent plateau), and contrasted to the conventional approach of donor-doping in BiVO₄ using metallic dopants such as tungsten (W). Our TRMC results also confirm that hydrogen treatment leads to the passivation of trap states and/or reduction of trap state density that act as recombination centers in BiVO₄. Through density functional theory (DFT) calculations, we show that the nature of these trap states is

likely to be associated with vanadium interstitials ($V_i^{\bullet\bullet\bullet\bullet}$) and vanadium anti-site on bismuth ($V_{Bi}^{\bullet\bullet}$). The carrier transport investigation was further extended to the early time window (< 2 ns) with THz conductivity measurements. Finally, we also quantified the amounts of hydrogen in hydrogen-treated BiVO_4 using ^{15}N nuclear reaction analysis (H-NRA). Our DFT analysis showed that hydrogen is bonded with oxygen (O-H) within the lattice of BiVO_4 , in agreement with an earlier NMR study on hydrogen-treated BiVO_4 .^[29]

2. Results and Discussions

Hydrogen treatment was performed on a spray-pyrolysed BiVO_4 thin film photoanode (see Experimental Section for detailed synthesis steps). Briefly, a pristine BiVO_4 sample was placed in a tube furnace under 2.4% H_2/Ar atmosphere for 10 min at 300 °C. **Figure 1a** shows the X-ray diffractograms of pristine and hydrogen-treated BiVO_4 films deposited on quartz substrates. Both films show only peaks representative of the pure monoclinic BiVO_4 phase (clinobisvanite; space group: $I2/a$, JCPDS card No. 014-0688). Slight shifts in the order of $0.1\text{-}0.2^\circ$ are observed in the (040), (200) and (002) peaks upon hydrogen treatment (Figure S1), indicating that the lattice is slightly distorted. These shifts have also been previously reported for tungsten-doped BiVO_4 , and can be considered as indicators for the successful incorporation of dopants.^[30] Raman spectroscopy was performed on the two BiVO_4 films, and the spectra are shown in Figure S2. The spectra are virtually identical, indicating that the short range order in the monoclinic BiVO_4 is not affected by hydrogen treatment. Finally, the optical characteristics of the BiVO_4 films do not seem to be affected significantly by our mild hydrogen treatment, as shown by the photographs and the UV-vis spectra of the films (Figure S3). Only a small increase of the absorbance is found for wavelengths above 500 nm. We do not believe this is due to increased scattering, since the microstructure of the film is not

expected to change during the mild H₂ treatment at 300°C. Instead, we attribute the increase to free electron absorption due to the fact that hydrogen in the bulk of BiVO₄ acts as a shallow donor. This will be discussed in more detail below. In summary, we observe no significant structural or optical changes upon hydrogenation of BiVO₄.

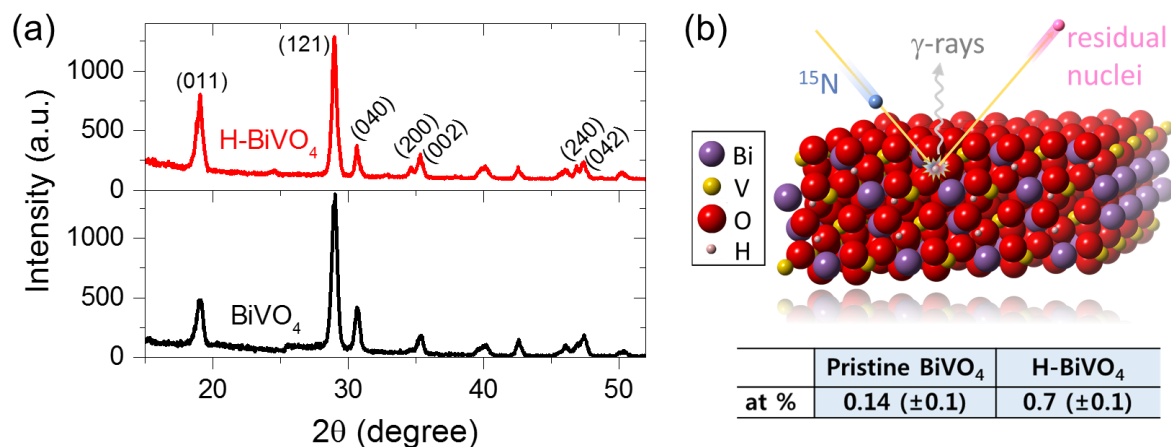


Figure 1. (a) X-ray diffractograms of pristine and hydrogen-treated (10 min. post-annealing in 2.4% H₂/Ar atmosphere at 300 °C) BiVO₄. (b) A schematic representation of the ¹⁵N nuclear reaction analysis (¹⁵N-NRA) on BiVO₄. The inset table shows the atomic content of hydrogen in pristine and hydrogen-treated BiVO₄.

To confirm the presence of hydrogen, we performed ¹⁵N nuclear reaction analysis (¹⁵N-NRA) on our films.^[31, 32] In short, the sample is bombarded with ¹⁵N ions (E > 6.385 MeV) that react with hydrogen according to the following equation:



The emitted γ -rays are detected and the measured intensity provides quantitative information on the amount of hydrogen present within the samples. As shown in **Figure 1b**, the hydrogen contents of pristine and hydrogen-treated BiVO₄ films were 0.14 ± 0.1% and 0.7 ± 0.1%, respectively. It should be mentioned that the hydrogen content measured by NRA may only

represent a certain fraction of total amount of hydrogen in the samples since the ion bombardment itself may result in removal of loosely bound hydrogen. Nevertheless, the measurements clearly show that the hydrogen treatment results in a significant increase of hydrogen content in BiVO₄. This result therefore provides direct and quantitative evidence that hydrogen is actually inserted into the BiVO₄ lattice upon hydrogen treatment, as opposed to only reducing the BiVO₄ to form oxygen vacancies.

We now turn our attention to the influence of hydrogen treatment on the photoelectrochemical performance of BiVO₄. **Figure 2** shows the AM1.5 photocurrent of pristine and hydrogen treated BiVO₄ films under back-side illumination. To exclude any surface catalytic limitations, sodium sulphite (Na₂SO₃) was added to the electrolyte as an effective hole scavenger.^[33] Hydrogen treatment results in a higher photocurrent plateau and a favourable cathodic shift of the onset potential of BiVO₄ (see Figure 2). We confirm that this improvement is a result of bulk modification of the BiVO₄ film by calculating the charge separation and charge injection efficiencies (Figure S4), using methods well described in the literature.^[34, 35] The charge separation efficiency increases with hydrogen treatment and matches the improvement in photocurrent. In contrast, the charge injection efficiency is found to decrease. It is currently unclear what causes the reduction of the charge injection efficiency. Recent experimental and theoretical studies on nickel oxyhydroxide revealed that its catalytic activity towards water oxidation is decreased by the presence of hydrogen on the surface.^[36]^{37]} The same effect may also occur in BiVO₄; further studies are needed to confirm this, which is beyond the scope of this paper.

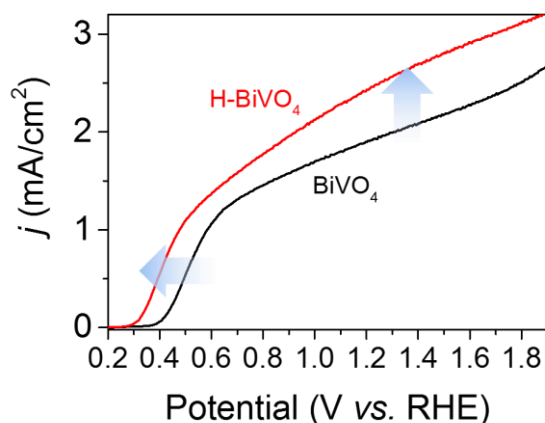


Figure 2. AM1.5 photocurrent-voltage (j - V) curves of pristine and hydrogen-treated BiVO_4 thin film photoanodes. Both the photocurrent plateau and onset potential are improved with hydrogen treatment. The electrolyte is 0.1 M phosphate buffer (KPi, pH \sim 7) and 0.5 M sodium sulphite (Na_2SO_3) as hole scavenger.

Our mild hydrogen treatment is also effective in improving the PEC performance of W-doped BiVO_4 and BiVO_4 prepared by other synthesis techniques. Figure S5 shows the AM1.5 photocurrent-voltage curves of a spray pyrolysed tungsten-doped BiVO_4 film as well as undoped BiVO_4 films prepared by magnetron sputtering and drop casting. In all cases, the photocurrent plateau increases and the onset potential shifts cathodically after hydrogen treatment. Thus, a hydrogen treatment appears to be a generally applicable strategy for improving the performance of BiVO_4 photoanodes, as has also been reported by others.^[24, 29, 38] Nevertheless, the main mechanism that causes the improvement of the PEC performance remains unclear.

To evaluate the influence of hydrogen treatment on the bulk carrier transport properties we utilized time-resolved microwave conductivity (TRMC).^[17, 39-42] In short, the BiVO_4 films are excited with a nanosecond laser pulse and the light-induced change in the reflected microwave power, which is sensitive to the presence of mobile carriers, is monitored (see Experimental Methods for more details). The TRMC signal can then be expressed as the

product of the absorbance-normalized quantum yield (ϕ) and the combined mobility of the charge carriers ($\Sigma\mu$, sum of the electron and hole mobilities). Assuming that the internal quantum yield of electron-hole generation approaches 100% and no charge carrier recombination has taken place within the response time of the setup, the carrier mobility (μ) and the carrier lifetime (τ) can be obtained from the peak and the decay of the TRMC signal, respectively.^[17, 40]

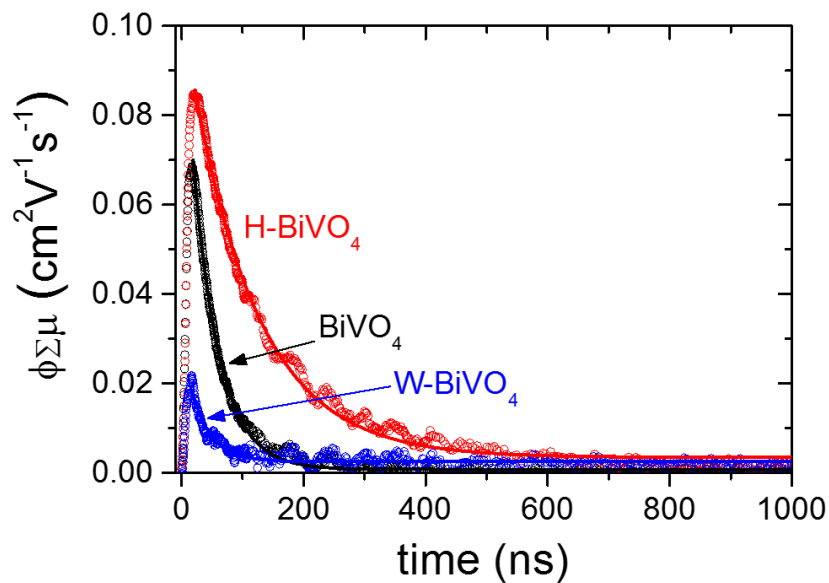


Figure 3. Time-resolved microwave conductivity signals recorded for pristine, hydrogen-treated and 1% tungsten-doped BiVO_4 thin films using a 355 nm laser pulse with a photon flux of 1.65×10^{12} photons cm^{-2} pulse $^{-1}$.

Figure 3 shows the TRMC signals ($\phi\Sigma\mu$ vs. time) for our BiVO_4 films under pulsed laser excitation of 355 nm with an intensity of 1.65×10^{12} photons cm^{-2} pulse $^{-1}$. For pristine BiVO_4 , a carrier mobility of ~ 0.07 $\text{cm}^2\text{V}^{-1}\text{s}^{-1}$ and a carrier lifetime of 43 ns is found. Upon hydrogen treatment, the carrier mobility slightly increases to ~ 0.08 $\text{cm}^2\text{V}^{-1}\text{s}^{-1}$ —the slight difference may be due to the fact that recombination is not zero within the response time of

our setup. Considering the effective mass of electron and hole in BiVO₄ (0.9 m₀ and 0.7 m₀, respectively)^[43], the individual electron (μ_e) and hole mobility (μ_h) of each films can be calculated (Table 1). The carrier lifetime, however, shows a much larger change and increases from 43 ns to 109 ns. The minority carrier diffusion length (L_h) can now be calculated using the following equations:

$$L_h = \sqrt{D_h \tau} \quad (2)$$

$$D_h = \frac{\mu_h kT}{e} \quad (3)$$

Here, k is the Boltzmann constant, T is the temperature, and e is the elementary charge. A value of 57 nm is found for the carrier diffusion length of untreated BiVO₄, which increases to 101 nm after hydrogen treatment (see Table 1). This improvement is consistent with the increased photocurrent plateau and improved charge separation we found for these hydrogen-treated BiVO₄ films.

Table 1. Carrier mobilities, lifetimes, and diffusion lengths of pristine, hydrogen-treated, and 1% tungsten-doped BiVO₄. All values were measured using a 355 nm laser pulse with a photon flux of 1.65×10^{12} photons cm⁻² pulse⁻¹.

Photoelectrode	μ (cm ² V ⁻¹ s ⁻¹)	μ_e (cm ² V ⁻¹ s ⁻¹)	μ_h (cm ² V ⁻¹ s ⁻¹)	τ (ns)	L_h (nm)
Pristine BiVO ₄	0.07	0.04	0.03	43	57
H-BiVO ₄	0.08	0.045	0.035	109	101
W-BiVO ₄	0.02	0.01	0.01	32	28

Since hydrogen has been suggested to act as a donor-type dopant in BiVO₄,^[24, 29] we compare the TRMC response with that for a tungsten-doped BiVO₄ film. Along with Mo, W is the most common effective donor dopant in BiVO₄.^[30, 34, 44] The TRMC signals and the extracted carrier properties of 1% W:BiVO₄ are shown in Figure 3 and Table 1. Consistent

with our earlier report^[17] and in contrast with the results on hydrogen-treated BiVO₄, W-doping in BiVO₄ results in a significantly smaller carrier mobility and lifetime.

To better understand the differences between H- and W-doping, we determined the carrier densities in both materials from electrical conductivity measurements (see Experimental Section and Supporting Information) and the TRMC-derived carrier mobilities. Interestingly, the carrier densities of both hydrogen-treated and tungsten-doped BiVO₄ are similar (see Table 2). The carrier density for the pristine BiVO₄ could not be calculated since we were unable to measure the resistivity of the film, possibly due to extremely high contact resistance. We therefore estimated the carrier density of the pristine BiVO₄ using dark microwave conductivity and Mott-Schottky measurements (Table 2, see Supporting Information for data and measurement details). Both tungsten doping and hydrogen treatment result in an increase of carrier density of ~2 orders of magnitude, which is higher than the factor of 5-20 increase of hydrogen content shown in Fig. 1b. We attribute this slight discrepancy to the increase of oxygen vacancy concentration upon hydrogen treatment, which is a reducing atmosphere. The increase of oxygen vacancies, however, is not responsible for the observed photocurrent improvement, as BiVO₄ film annealed in Ar (without H₂) does not show any changes in photocurrent as compared to the untreated film (Figure S6).

Table 2. Two-electrode ac electrical conductivity data for hydrogen-treated and 1% tungsten-doped BiVO₄. The resistance was measured between gold (Au) contacts deposited on the surface of the film with varying pitch distance, with dc bias of 1 V, ac amplitude of 10 mV, and frequency of 1 MHz. *No conductivity data can be obtained from the pristine BiVO₄, possibly due to extremely high contact resistance. The carrier density value for the pristine BiVO₄ was therefore estimated using dark microwave conductivity and Mott-Schottky measurements. Details of the electrical conductivity, dark microwave conductivity and Mott-Schottky measurements are shown in the Supporting Information (Supporting Note).

Photoelectrode	Resistivity ρ ($\Omega \cdot \text{m}$)	Conductivity σ (10^3 S m^{-1})	Carrier density N_d (cm^{-3})
Pristine BiVO ₄	-	-	$7.0 \pm 1.7 \times 10^{18}$ *
H-BiVO ₄	$0.8 \pm 0.3 \times 10^{-3}$	1.40 ± 0.3	$1.1 \pm 0.3 \times 10^{21}$
W-BiVO ₄	$2.4 \pm 0.7 \times 10^{-3}$	0.45 ± 0.1	$2.9 \pm 0.8 \times 10^{21}$

The results above indicate that although both tungsten doping and hydrogen treatment increase the carrier concentration in BiVO₄, the effect on the carrier transport properties is completely different. The decrease of mobility and lifetime in the tungsten-doped BiVO₄ has been attributed to the formation of trap states.^[17] To investigate the possible change in these trap states after hydrogen treatment, the TRMC signals ($\phi \sum \mu$) of both pristine and hydrogen-treated BiVO₄ were obtained at different laser pulse intensities, as shown in **Figure 4**. For pristine BiVO₄, the $\phi \sum \mu$ increases with light intensity until it reaches a maximum at $\sim 2 \times 10^{12}$ photons pulse⁻¹ cm⁻². Beyond this light intensity, $\phi \sum \mu$ decreases with increasing light intensity. This behavior has also been reported elsewhere,^[17, 39, 45, 46] and it has been attributed to the competition between electron trap filling and higher-order recombination. At such, it has been used as a signature for the presence of trap states in semiconductors (i.e., trap-assisted recombination). At lower light intensities, the concentration of trap states is higher than the

number of absorbed photons; therefore, $\phi_{\Sigma\mu}$ increases with light intensity until all the trap states are filled. At this point, no further trapping can occur, and $\phi_{\Sigma\mu}$ will reach a maximum. Beyond that, the signal decreases with higher light intensity due to fast non-geminate higher-order recombination during the laser pulse.^[47] The same intensity dependence of $\phi_{\Sigma\mu}$ is, however, not found in the hydrogen-treated BiVO₄ (Figure 4). With increasing light intensity, only the signature of the fast non-geminate higher-order recombination is detected, i.e., $\phi_{\Sigma\mu}$ decreases continuously. No maximum is observed in the trend, indicating that only few trap states are present after the hydrogen treatment. We finally note that the behavior for the here-reported pristine BiVO₄ is different from our previous report.^[17] We attribute this to small changes we recently had to make to our spray deposition setup (see Experimental Section), which may result in larger concentration of trap states.

The observed reduction of trap states density upon hydrogen treatment is in agreement with a recent report by Cooper et al.,^[29] where hydrogen-treated BiVO₄ was found to exhibit a lower sub-bandgap photoluminescence intensity as compared to untreated BiVO₄. The reduction in the number of trap states is also consistent with the increase in carrier lifetimes (Figure 3 and Table 1), which in turn results in the cathodic shift of the onset potential in the photocurrent-voltage curve (Figure 2). To confirm the relationship between carrier lifetime and onset potential, we simulated a set of photocurrent-voltage curves for varying carrier lifetimes using a model developed by Reichman.^[48] Reichman's model is an extension of the well-known Gärtner model, using more appropriate boundary conditions for the derivation of the valence band photocurrent and allowing for the possibility of recombination in the space charge region. As shown in Figure S7, the photocurrent onset potential indeed shifts cathodically with increasing carrier lifetime.

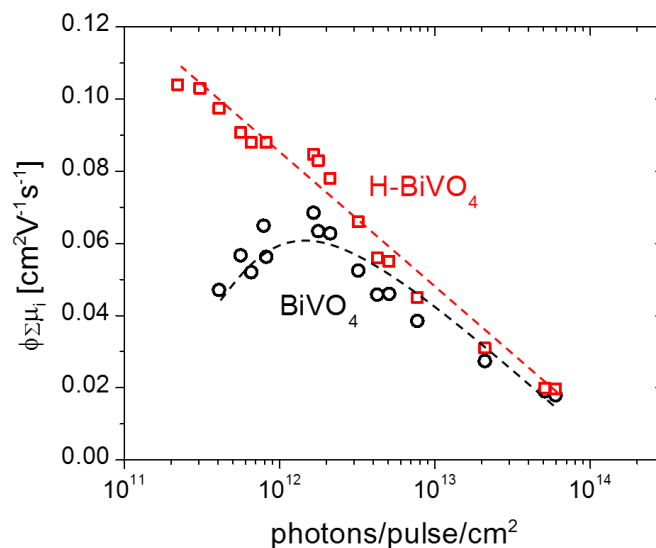


Figure 4. Maximum observed TRMC signals as a function of incident photons for pristine and hydrogen-treated BiVO₄. AM1.5 illumination is equivalent to an incident number of photons of $\sim 10^9$ pulse⁻¹ cm⁻².

To understand the nature of the trap states that are significantly decreased upon hydrogen treatment, we performed density functional theory (DFT) calculations using a $2 \times 1 \times 2$ supercell model of the monoclinic structure of BiVO₄, consisting of 16 functional units of BiVO₄ (i.e., Bi₁₆V₁₆O₆₄). Detailed information about the DFT methodology adopted for this work can be found in the Experimental Methods section. Although several DFT studies are available in the literature,^[24, 49] they were performed under different processing conditions and assumed charged defects prior to the calculation. In our methodology, we considered as initial guess (i.e., before structural optimization) neutral defects, and the formation energies were then computed by taking into account the thermal parts of the oxygen and hydrogen chemical potentials at pressure and temperature mimicking our deposition and annealing conditions. This method has been successfully applied to investigate the thermodynamic stability of various defective (photo-)catalytic materials, and was shown to be well in-line with experimental observations.^[50-55]

Table 3 summarizes the calculated formation energy of defects in both unmodified and hydrogen-treated BiVO₄. Among the various intrinsic defects explored, only those corresponding to interstitial vanadium ($V_i^{\bullet\bullet\bullet\bullet}$) and vanadium anti-site on bismuth ($V_{Bi}^{\bullet\bullet}$) are found to have relatively low formation energies (less than 100 meV). Upon insertion of hydrogen, the formation energies of both point defects were found to increase, indicating a smaller likelihood of their formation. In contrast, other point defects showed lower formation energies (i.e., easier formation) upon insertion of hydrogen.

Table 3. Calculated formation energies for the various explored defective structures before and after hydrogenation. The point defects are expressed in Kröger-Vink notations.^[56] $V_{Bi}^{///}$: bismuth vacancy, $V_V^{////}$: vanadium vacancy, $V_O^{\bullet\bullet}$: oxygen vacancy, $Bi_i^{\bullet\bullet\bullet}$: bismuth interstitial, $V_i^{\bullet\bullet\bullet\bullet}$: vanadium interstitial, $O_i^{//}$: oxygen interstitial, $Bi_V^{//}$: bismuth anti-site on vanadium, and $V_{Bi}^{\bullet\bullet}$: vanadium anti-site on bismuth.

Point defects	Formation energy in BiVO ₄ (eV) ^{a)}	Formation energy in H-BiVO ₄ (eV) ^{b)}
$V_{Bi}^{///}$	0.467	0.364
$V_V^{////}$	0.967	0.781
$V_O^{\bullet\bullet}$	0.277	0.268
$Bi_i^{\bullet\bullet\bullet}$	0.394	0.391
$V_i^{\bullet\bullet\bullet\bullet}$	0.041	0.072
$O_i^{//}$	0.201	0.179
$Bi_V^{//}$	0.446	0.402
$V_{Bi}^{\bullet\bullet}$	0.024	0.068

^{a)}T = 723 K in O₂ atmosphere; ^{b)}T = 723 K in O₂ atmosphere and 573 K in H₂ atmosphere;

Formation energies at 0 K are shown in Table S1.

In addition to decreased trap states density, passivation of trap states (i.e., modification of their electronic states) may also explain the improved carrier transport properties upon

hydrogen treatment. We therefore further analyzed the structural parameters, atomic environments and the corresponding electronic density of states (DOS) of the $V_i^{\bullet\bullet\bullet\bullet}$ - and $V_{Bi}^{\bullet\bullet}$ - containing BiVO_4 . The lattice parameters and chemical bonds are shown in Table S2, and the detailed atomic structures are depicted in **Figure 5**. The calculated DOS diagrams are shown in Figure S8. For the $V_i^{\bullet\bullet\bullet\bullet}$ -containing BiVO_4 , the vanadium interstitial is octahedrally coordinated with neighboring oxygen atoms (bond lengths 1.95-2.09 Å). It is also surrounded by 3 neighboring vanadium atoms at distances of 2.39 and 2.74 Å and by 2 neighboring bismuth atoms at a distance of 3.0 Å (Figure 5a, left). The most stable spin configuration is found to be an open-shell quartet state with the spin density partially located on the inserted vanadium. This results in new defect states within the bandgap of BiVO_4 , as shown in Figure S8b. Inserting hydrogen into this structure results in the formation of a 0.98 Å long O-H bond with one oxygen bridging the interstitial vanadium and one of the 3 neighboring vanadium atoms (Figure 5a, right). The most stable spin configuration for this structure is increased to a quintet state. The new electron introduced upon hydrogen insertion is mainly localized on the neighboring vanadium, leading to an increase of the local spin density on this vanadium from 0.38 to 1.1. This localization leads to minimal change of the energetic position of these states, as shown in Figure S8c. Hydrogen treatment therefore is not expected to cause passivation of $V_i^{\bullet\bullet\bullet\bullet}$.

For the $V_{Bi}^{\bullet\bullet}$ -containing BiVO_4 , the $V_{Bi}^{\bullet\bullet}$ anti-site defect is tetrahedrally coordinated with neighboring oxygen ions with bond lengths ranging from 2.01 to 2.02 Å (Figure 5b, left). The most stable spin configuration is found to be an open-shell triplet state in which almost the whole spin density is localized on the substitutional vanadium, also giving rise to new defect states within the bandgap of BiVO_4 (Figure S8d). Addition of hydrogen in this structure results in the formation of an O-H bond of 1.01 Å with the oxygen atom far from the defective region (Figure 5b, right). The most stable spin configuration for this structure is increased to a

quartet state, with the new electron introduced upon hydrogen insertion fully delocalized throughout the whole crystal. Prior to hydrogen treatment, the electron localized on the inserted vanadium anti-site on bismuth is 1.8 (vs. 2.0 in total for an open-shell triplet state); insertion of hydrogen results in 2.2 localized electrons (vs. 3.0 in total for a quartet state). The ratio of localized electrons is therefore decreased upon hydrogen treatment (from 0.9 to 0.73). As a result of this delocalization, the defect states shift towards the bottom of the conduction band (Figure S8e), i.e., the defect states become shallower. Therefore, differently from the vanadium interstitial, insertion of a hydrogen atom in the $V_{Bi}^{\bullet\bullet}$ -containing $BiVO_4$ also results in the passivation of the defect states.

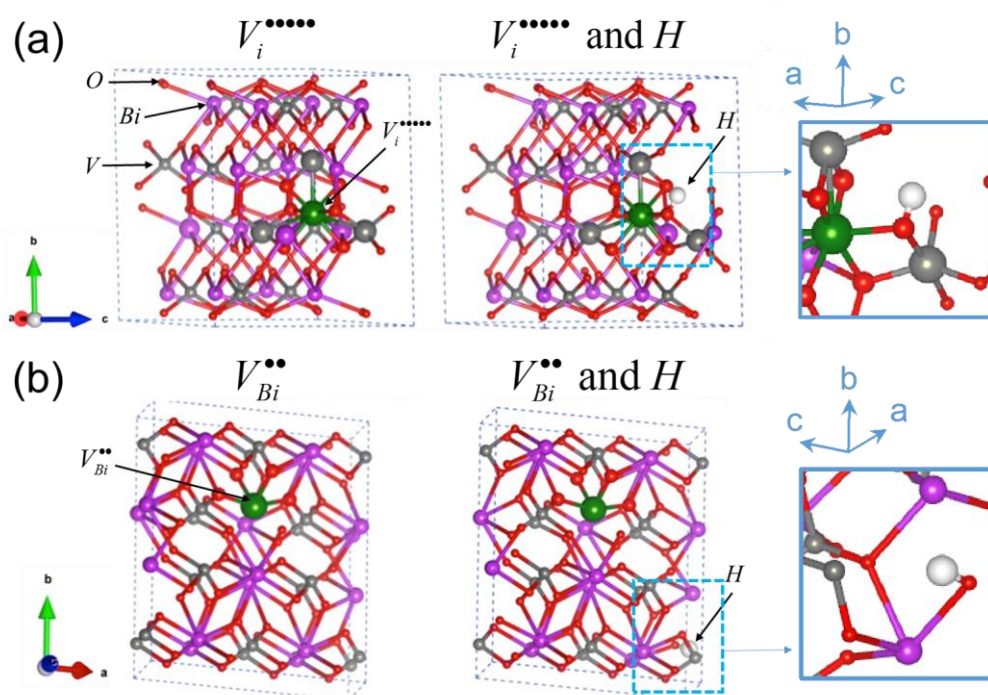


Figure 5. Optimized structures of $2 \times 1 \times 2$ $BiVO_4$ supercell with (a) one interstitial V and (b) one substitutional V at Bi site, before (left) and after (middle) inserting one hydrogen. Bi atoms are shown in purple, V in gray, O in red and H in white. Interstitial or substitutional V is shown in green. The magnifications of hydrogen position in the lattice are shown respectively on the right.

Based on the above DFT results, we propose that the nature of the trap state in BiVO₄ affected by hydrogen treatment is vanadium interstitial ($V_i^{\bullet\bullet\bullet\bullet}$) and/or vanadium anti-site on bismuth ($V_{Bi}^{\bullet\bullet}$). Upon hydrogen treatment, the concentrations of $V_i^{\bullet\bullet\bullet\bullet}$ and $V_{Bi}^{\bullet\bullet}$ in BiVO₄ are reduced as evident from the higher formation energies. In the case of $V_{Bi}^{\bullet\bullet}$, the reduction of the density is accompanied by an upward shift of the energetic position of the defect states, i.e., passivation of the states. Overall, these result in superior carrier transport properties, especially the carrier lifetime. Further experimental studies beyond the scope of this paper are needed to distinguish the influence of hydrogen treatment to these two defects in BiVO₄.

Finally, we also investigated if the inserted hydrogen would have an impact on the carrier transport at an earlier time window (< 2 ns) using time-resolved THz conductivity (TRTC) measurements. We excited our BiVO₄ samples with a femtosecond laser pulse and used a low probe photon energy of only a few meV to detect the mobile carriers. The THz photoconductivity transients of pristine and hydrogen-treated BiVO₄ are shown in **Figure 6a**. A minor variation of decay times is observed in the first tens of picoseconds, but overall no significant differences can be observed at this time window (see Figure 6a inset). We have previously shown that the decay in BiVO₄ in this time window is related to continuous reduction of carrier mobility, as opposed to recombination of carriers that occurs at time scales >10 ns.^[57] Figure 6a therefore directly represents the carrier mobilities in each sample, on which the hydrogen treatment clearly does not have a significant impact. This is consistent with our TRMC results, which revealed comparable carrier mobility values for bare and hydrogen-treated BiVO₄ (see Table 1).

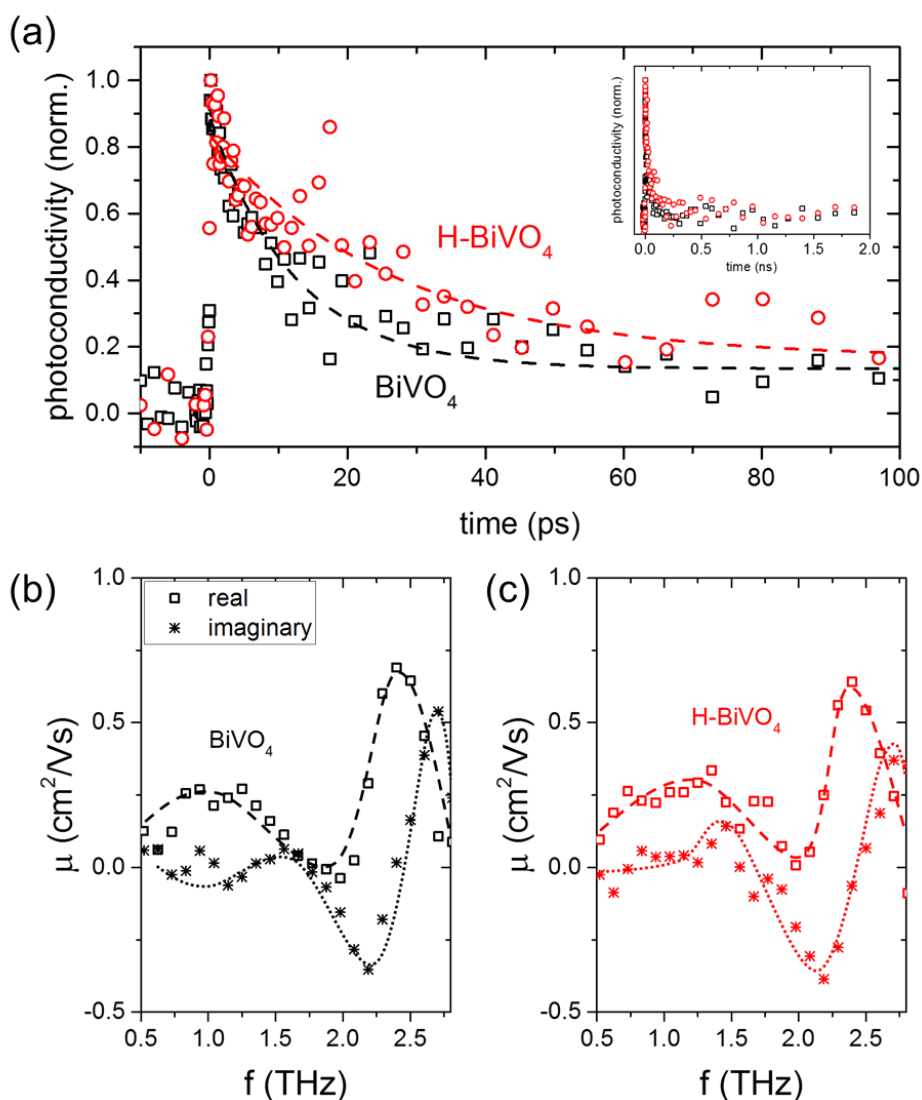


Figure 6. (a) THz photoconductivity transients of bare and hydrogen-treated BiVO₄ films in a time window of < 100 ps. The dashed lines represent single exponential fits to the data as a guide for the eye. The transients for longer time window (up to 2 ns) are shown in the inset. THz combined electron-hole mobility spectra of (b) pristine and (c) hydrogen-treated BiVO₄ measured at delay time of 20 ps. The open squares represent the real data points and stars the imaginary data points. The dashed and dotted lines are guides to the eye for the real and imaginary spectra, respectively.

An additional advantage of TRTC is the possibility to distinguish between free and weakly bound (i.e., localized) charge carriers.^[58-60] In fact, we recently reported direct time-

resolved evidence of small hole polaron formation in BiVO₄ using THz spectroscopy.^[57] There, we observed a resonance peak in the mobility-THz frequency spectrum, which is indicative of strong carrier localization. This was corroborated by observation of a phonon mode in the Raman spectrum at $\sim 70\text{ cm}^{-1}$, which corresponds well with the resonant frequency of $\sim 2.3\text{ THz}$. This phonon mode has been assigned to an external (Bi³⁺-VO₄³⁻) vibration along the [012] or [102] axes.^[57, 61] Our DFT calculations (Table S2) suggest that hydrogen treatment causes additional distortion to the BiVO₄ lattice, which results in a slight increase of the bond distance along these two external vibration axes ([012] and [102]). Indeed, we observe a 3 cm^{-1} (equivalent to $\sim 0.09\text{ THz}$) shift of the Raman peak to a lower wavenumber upon hydrogen treatment (Figure S9). **Figure 6b and c** shows the THz mobility spectra of both pristine and hydrogen-treated BiVO₄ at probe delay time of 20 picoseconds. In both cases, a modified Drude-Smith conductivity model can be used to describe the spectra below 1.7 THz, whereas a damped oscillator model fits well for the spectra above 1.7 THz. No significant differences are observed in term of both the spectral shape as well as the amplitude between the two BiVO₄ films (the expected $\sim 0.09\text{ THz}$ shift is smaller than the resolution of our measurement). Consistent with the TRMC results, a carrier mobility value of $\sim 0.10\text{ cm}^2\text{V}^{-1}\text{s}^{-1}$ is obtained by extrapolating the THz mobility spectrum to the y-axis (see Figure S10). Hydrogen treatment therefore does not seem to affect the nature of the conductivity in BiVO₄. In addition, since hole polaron formation is not affected by the hydrogen treatment, we can conclude that the trap states described above are located energetically deeper than the polaron states. Holes then exit the polaron state (Figure S11) and start recombining or further trapped at lower states at time scales $> 2\text{ ns}$; combined with the reduced trap state density and passivation of trap states, this results in longer carrier lifetime as observed with TRMC measurements.

3. Conclusion

In summary, a mild hydrogen treatment (2.4% H₂ in Ar, 300 °C, 10 mins) results in a significant increase of the carrier lifetime in BiVO₄ photoanodes, while the carrier mobility remains unaffected. The longer lifetime is attributed to the reduction and passivation of deep trap states that act as recombination centers. The opposite is shown for tungsten-doped BiVO₄, despite hydrogen also being a donor-type dopant. DFT calculations have identified vanadium interstitials and vanadium anti-site on bismuth as likely candidates for these trap states. As a result of the improved carrier lifetime, the photoelectrochemical performance of the hydrogen-treated BiVO₄ is significantly improved: the photocurrent plateau increases by ~25% and the onset potential is shifted cathodically by ~100 mV. Nuclear reaction analysis provided direct evidence for the presence of ~0.7 at% hydrogen in the lattice of hydrogen-treated BiVO₄. The incorporated hydrogen forms O-H bonds and distorts the lattice of BiVO₄, which results in a slight shift of Bi³⁺-VO₄³⁻ external vibration peak. This additional distortion, however, does not affect the hole polaron formation, which means that the trap states are energetically located deeper than the hole polaron states. These results represent an important step forward in our understanding of the carrier transport properties in BiVO₄ and possible defect passivation/reduction strategies. Similar considerations are likely valid for other metal oxides, and will thus benefit further development of highly efficient photoelectrodes for solar energy conversion.

4. Experimental Section

Synthesis: BiVO₄ thin films were prepared by spray pyrolysis on quartz (2.5 x 1.2 cm², Spectrosil® 2000, Heraeus). Detailed information on the basic spray pyrolysis setup and precursor can be found in the literature;^[34, 62, 63] the only difference is a minor modification of the air atomizing spray head (Quickmist 1/4QMJAU-NC + SUQR200), since the original

spray head is no longer carried by the supplier. In short, the quartz substrate was placed on a hot plate, and its temperature was maintained at 450°C during the spray pyrolysis of BiVO₄. 200 cycles of deposition were performed with the rate of ~1 nm per each cycle. Finally, the BiVO₄ film was post annealed for 2 hours at 450°C in air. For PEC measurements, FTO-coated glass (TEC-15, Pilkington) was used as the substrate instead of quartz. Hydrogen-treated BiVO₄ (H-BiVO₄) samples were obtained by a simple annealing of bare BiVO₄ under 2.4% H₂ in Ar (Arcal10, Air Liquide) for 10 min at 300 °C. Tungsten-doped BiVO₄ (W-BiVO₄) films were obtained by introducing 1 at% of tungsten ethoxide, W(OC₂H₅)₆, into the initial precursor solution.^[11, 34]

Materials Characterization: Photoelectrochemical characterization was carried out in a three-electrode configuration. Electrical contact to the sample was made using a copper wire and conducting tape (tin-plated copper foil with conductive adhesive, 3M™ 1183). The potential of the working electrode (i.e., the sample) was controlled by a potentiostat (EG&G PAR 273A). A Pt wire and an Ag/AgCl electrode (XR300, saturated KCl and AgCl solution, Radiometer Analytical) were used as the counter and reference electrodes, respectively. The electrolyte was a 0.1 M potassium phosphate (KPi) buffer solution, pH ~7, with added 0.5 M sodium sulphite (Na₂SO₃) in demineralized and deionized water (18.2 MΩ.cm). Cyclic voltammetry measurements were performed with a scan rate of 50 mV/s. White light photocurrent measurements were performed under AM1.5 solar illumination (100 mW/cm²) with a solar simulator (WACOM, type WXS-50S-5H, class AAA).

Structural analysis was performed with a Bruker D8 Advance X-ray diffractometer (Cu-K_α, λ = 0.154056 nm) in the grazing incidence configuration. Ultraviolet-visible absorption data were measured with a Perkin Elmer Lambda 950 spectrometer. Raman spectroscopy was performed using a Horiba HR800 spectrometer with a HeNe laser excitation wavelength of

632.82 nm. Nuclear reaction analysis was performed at the Ion Beam Center of Helmholtz-Zentrum Dresden Rossendorf, Germany. The samples were bombarded with doubly charged nitrogen ions with an incident angle of 45° and an incident energy of 6425 keV (ion penetration depth ~ 20 nm). The measured amount of hydrogen represents the fraction of tightly-bounded hydrogen since the ion bombardment may result in (partial) removal of loosely-bounded hydrogen.

For the resistivity measurement, BiVO_4 is coated on quartz by spray pyrolysis, followed by electron beam evaporation of gold (Au) using a mask to create well defined contacts (Figure S12). Details on the measurement configuration, setup and procedures are shown in the Supporting Information (Supporting Note). Dark microwave conductivity was also used to estimate the carrier concentration (data and procedures are shown in the Supporting Note). Electrochemical impedance and Mott-Schottky measurements were performed using a VERSASTAT 3F potentiostat.

Time-resolved spectroscopy: Time-resolved microwave conductivity (TRMC) measurements were performed by mounting the samples in a microwave cavity cell and placed within a setup similar to the one described elsewhere.^[39, 40] During the measurements, a change in the microwave power reflected by the cavity upon sample excitation by 6 ns (full-width at half-maximum) pulses of a frequency-tripled Q-switched Nd:YAG laser at a wavelength of 355 nm (10 Hz repetition rate), $\Delta P/P$, was monitored and correlated to the photoinduced change in the conductance of the sample, ΔG , by

$$\frac{\Delta P}{P}(t) = -K\Delta G(t) \quad (4)$$

where K is the sensitivity factor derived from the resonance characteristics of the cavity and the dielectric properties of the medium (ϵ_r of BiVO_4 is taken as $68^{[30]}$). From the experimentally observed change in the photoconductance, the product of the charge carrier

generation yield (ϕ) and the sum of electron and hole mobilities ($\Sigma\mu$) can be obtained according to

$$\phi\Sigma\mu = \frac{\Delta G}{I_0\beta eF_A} \quad (5)$$

where I_0 is the incident intensity per pulse, e is the elementary charge, β is the ratio between the inner broad and narrow dimensions of the waveguide, and F_A is the fraction of incident photons absorbed within the sample. The laser pulse intensities were adjusted by the use of calibrated filters and varied from $\sim 10^{11}$ to 10^{14} photons cm^{-2} pulse $^{-1}$.

THz spectroscopy was performed by connecting the THz spectrometer to a femtosecond laser system consisting of a 150 kHz amplifier (RegA, Coherent) seeded by 800 nm pulses of a Ti:sapphire 80 MHz oscillator (Mira, Coherent), yielding 7 μJ pulses with autocorrelation lengths of ~ 70 fs (fwhm). The laser output is split into three branches which are used for THz generation, THz detection and the optical excitation of the sample at the frequency-doubled wavelength of 400 nm. Further details of the experimental setup have been described previously.^[64] The THz pulse is generated by optical rectification in a ZnTe crystal. A series of parabolic mirrors guide the THz probe pulse onto the sample and focus the transmitted signal onto the detection sequence based on electro-optic sampling. The available experimental spectral range is from 0.5 to 3 THz. An InP reference sample with known signal yield is measured within every experimental slot to ensure proper functioning of the spectrometer.

Density functional theory (DFT): Intrinsic defects in pristine BiVO_4 were examined using a $2 \times 1 \times 2$ supercell model of the monoclinic structure of perfect BiVO_4 (point group: C_6^2h , space group: C2/c), which consists of two unit cells stacked both along the a - and c -axes (16 functional units $\text{Bi}_{16}\text{V}_{16}\text{O}_{64}$ or 96 atoms) and has sufficient length to avoid the self-interactions of the defect along each direction. Several structural configurations for intrinsic

defects, namely Bi-vacancy, V-vacancy, O-vacancy, Bi-interstitial, V-interstitial, O-interstitial, Bi on V site and V on Bi site, were modeled. For Bi-, V- and O-deficient BiVO_4 , one Bi, V or O atom was removed from the $\text{Bi}_{16}\text{V}_{16}\text{O}_{64}$ supercell and labeled by their respective point defect Kröger-Vink notations: $V_{\text{Bi}}^{///}$, $V_{\text{V}}^{////}$ or V_{O}^{**} . For Bi-, V- or O-enriched BiVO_4 , one neutral Bi, V or O atom was inserted into the $\text{Bi}_{16}\text{V}_{16}\text{O}_{64}$ supercell and labeled by Bi_i^{***} , V_i^{****} or $O_i^{//}$. Moreover, one Bi atom was substituted at one V site (labeled by $\text{Bi}_V^{//}$) into the $\text{Bi}_{16}\text{V}_{16}\text{O}_{64}$ supercell as well as one substitutional V at Bi site (labeled by V_{Bi}^{**}) was considered. For each type of defect, a large number of configurations were generated in order to find the most stable structure. The preferential location of H in hydrogenated BiVO_4 was also investigated by inserting one H atom at various possible sites into the Bi-, V-, O-deficient or enriched $\text{Bi}_{16}\text{V}_{16}\text{O}_{64}$ supercell models invoked above. All the structures considered in this work were fully optimized by means of the spin-polarized periodic density functional theory (DFT) within the plane wave (PW) approach using the VASP software.^[65-68] The generalized gradient approximation (GGA) within the Perdew-Burke-Ernzerhof (PBE) exchange-correlation functional^[69] and the standard frozen-core projector augmented-wave (PAW) approach^[70] were employed to describe the electron-electron and the electron-ion interactions, respectively. The valence electron configurations taken into account in PAW potentials are $6s^26p^3$ for Bi, $3p^63d^44s^1$ for V, $2s^22p^4$ for O and ultrasoft $1s^1$ for H. A cutoff energy of 400 eV was used for basis functions. In all cases, the Brillouin zone was sampled with $3 \times 3 \times 3$ Monkhorst-Pack k -point grid.^[71] The relaxation run was considered converged when the force components on each species were less than $0.01 \text{ eV}/\text{\AA}$, the stress was less than 0.02 GPa, the displacement was less than $5 \times 10^{-4} \text{ \AA}$, and the energy change per species was less than $5 \times 10^{-6} \text{ eV}$. As the magnetic state depends on the type of defect, several spin multiplicities were tested for each defective configuration in order to identify the most stable spin electronic state.

The relative stability of the various explored self-defective BiVO₄ materials before and after hydrogenation with respect to the perfect one was investigated by computing the defect formation energies using the four following expressions:

$$E_{form}(1) = E_{tot} [Bi_{(1-x)}V_{(1-y)}O_{(4-z)}H_t] - E_{tot} [BiVO_4] + x.E_{tot} [Bi] + y.E_{tot} [V] + \frac{z}{2}.E[O_2] - \frac{t}{2}.E[H_2] + z.\Delta\mu_O - t.\Delta\mu_H \quad (9)$$

$$E_{form}(2) = E_{tot} [Bi_{(1+x)}V_{(1+y)}O_{(4+z)}H_t] - E_{tot} [BiVO_4] - x.E_{tot} [Bi] - y.E_{tot} [V] - \frac{z}{2}.E[O_2] - \frac{t}{2}.E[H_2] - z.\Delta\mu_O - t.\Delta\mu_H \quad (10)$$

$$E_{form}(3) = E_{tot} [Bi_{(1+x)}V_{(1-y)}O_4H_t] - E_{tot} [BiVO_4] - x.E_{tot} [Bi] + y.E_{tot} [V] - \frac{t}{2}.E[H_2] - t.\Delta\mu_H \quad (11)$$

$$E_{form}(4) = E_{tot} [Bi_{(1-x)}V_{(1+y)}O_4H_t] - E_{tot} [BiVO_4] + x.E_{tot} [Bi] - y.E_{tot} [V] - \frac{t}{2}.E[H_2] - t.\Delta\mu_H \quad (12)$$

$E_{tot}[BiVO_4]$, $E_{tot}[Bi_{(1-x)}V_{(1-y)}O_{(4-z)}H_t]$, $E_{tot}[Bi_{(1+x)}V_{(1+y)}O_{(4+z)}H_t]$, $E_{tot}[Bi_{(1-x)}V_{(1+y)}O_4H_t]$ and $E_{tot}[Bi_{(1+x)}V_{(1-y)}O_4H_t]$, $E_{tot}[Bi]$ and $E_{tot}[V]$ are the total energies of the pure and self-defective solids in their most stable structures while $E[O_2]$ and $E[H_2]$ represent the total energies for these two molecules in gas phase. $\Delta\mu_O$ and $\Delta\mu_H$ are the thermal parts of the oxygen and hydrogen chemical potentials which depends on temperature (T) and pressure (p) via the enthalpy (h) and entropy (s) corrections as follows:

$$\Delta\mu_O = h_{O_2}(T) - Ts_{O_2}(T) + RT \ln \left(\frac{p[O_2]}{p_0} \right) \quad (13)$$

$$\Delta\mu_H = h_{H_2}(T) - Ts_{H_2}(T) + RT \ln \left(\frac{p[H_2]}{p_0} \right) \quad (14)$$

The zero point vibrational energy, the enthalpy correction (h) and the entropy (s) of O_2 and H_2 as a function of the temperature (T) and the pressure (p) were calculated using DMol program^[72] within the PBE exchange-correlation functional and the DNP basis set.^[73] The

zero point vibrational energy was systematically included in the enthalpy and entropy corrections. The thermal contributions of the solids were neglected. All electronic energies (for solids and molecules) were calculated using VASP program. In what follows, $\Delta\mu_o$ was set at -0.67 eV for $T = 723$ K and $\Delta\mu_H$ at -0.26 eV for $T = 573$ K with 1 atm pressure to mimic the experimental conditions. Higher or lower defect formation energy represents less or more stable material than the perfect BiVO_4 one. Note that the defect formation energy for $V_{Bi}^{///}$ upon hydrogenation was obtained from Equation 9 for $y = z = 0$ and $x = t = 1/16$, whereas those for $V_V^{////}$ and V_O^{**} were also obtained from Equation 9 for $x = z = 0$; $y = t = 1/16$ and for $x = y = 0$; $z = t = 1/16$, respectively. For Bi_i^{***} , the defect formation energy upon hydrogenation was obtained from Equation 10 for $y = z = 0$ and $x = t = 1/16$, whereas those for V_i^{*****} and $O_i^{//}$ were also obtained from Equation 10 for $x = z = 0$; $y = t = 1/16$ and for $x = y = 0$; $z = t = 1/16$, respectively. For V_{Bi}^{**} , the defect formation energy upon hydrogenation was obtained from Equation 11 for $x = y = t = 1/16$, whereas that for $Bi_V^{//}$ was obtained from Equation 12 for $x = y = t = 1/16$. Note the formation energies of the various explored intrinsic defects in the pristine BiVO_4 material were obtained using the same equations for $t = 0$.

The electronic properties of pristine and the most relevant self-defective BiVO_4 materials were examined through density of states (DOS) calculations shown in Figure S8 in the Supporting Information. The calculations were conducted by means of the spin-polarized DFT based on the fully optimized geometries using the PBE functional as implemented in VASP software. The tetrahedron method with Blöchl corrections was adopted for integrating the Brillouin zone. An increased cutoff energy of 500 eV was used for basis functions to ensure the sufficient convergence of the band gap values of these materials. For electronic structure calculations of semiconductors, it is well known that GGA functionals such as PBE underestimate the absolute experimental band gap values, and this can be greatly corrected by

the use of range-separated hybrid Heyd-Scuseria-Ernzerhof (HSE06) functional.^[50-52, 74-80] However, our main focus on this study was to show the trend rather (relative difference) rather than giving absolute numbers. A systematic computational investigation of the impact of relevant self-intrinsic defects on the optoelectronic properties of BiVO₄ at the HSE06 level of theory is indeed under progress and will be reported soon.

Supporting Information

Supporting Information is available from the Wiley Online Library or from the author.

Acknowledgements

This research was supported by the PECDEMO project (co-funded by Europe's Fuel Cell and Hydrogen Joint Undertaking under Grant Agreement no. 621252) and the German Bundesministerium für Bildung und Forschung (BMBF), project 'MeOx4H2' (03SF0478A). Parts of this research were carried out at IBC at Helmholtz-Zentrum Dresden-Rossendorf e.V., a member of the Helmholtz Association. The authors thank Dr. Klaus Ellmer and Karsten Harbauer for the assistance in the electrical conductivity measurements. Present address of Dr. J.-W. Jang: School of Energy and Chemical Engineering, Ulsan National Institute of Science and Technology (UNIST), Ulsan, 44919 South Korea

Received: ((will be filled in by the editorial staff))

Revised: ((will be filled in by the editorial staff))

Published online: ((will be filled in by the editorial staff))

References

- [1] M. I. Hoffert, K. Caldeira, A. K. Jain, E. F. Haites, L. D. D. Harvey, S. D. Potter, M. E. Schlesinger, S. H. Schneider, R. G. Watts, T. M. L. Wigley, D. J. Wuebbles, *Nature* **1998**, 395, 881.
- [2] N. S. Lewis, D. G. Nocera, *Proc. Natl. Acad. Sci. USA* **2006**, 103, 15729.
- [3] J. M. Ogden, *Annu. Rev. Energy Env.* **1999**, 24, 227.
- [4] A. Haryanto, S. Fernando, N. Murali, S. Adhikari, *Energy & Fuels* **2005**, 19, 2098.
- [5] M. Grätzel, *Nature* **2001**, 414, 338.
- [6] R. van de Krol, M. Grätzel, *Photoelectrochemical Hydrogen Production*, Springer, **2012**.
- [7] O. Khaselev, J. A. Turner, *Science* **1998**, 280, 425.
- [8] S. Licht, *J. Phys. Chem. B* **2001**, 105, 6281.
- [9] M. M. May, H.-J. Lewerenz, D. Lackner, F. Dimroth, T. Hannappel, *Nat. Commun.* **2015**, 6:8286.
- [10] J. H. Kim, J.-W. Jang, Y. H. Jo, F. F. Abdi, Y. H. Lee, R. van de Krol, J. S. Lee, *Nat. Commun.* **2016**, 7:13380.
- [11] F. F. Abdi, L. Han, A. H. M. Smets, M. Zeman, B. Dam, R. van de Krol, *Nat. Commun.* **2013**, 4:2195.

- [12] Y. Pihosh, I. Turkevych, K. Mawatari, J. Uemura, Y. Kazoe, S. Kosar, K. Makita, T. Sugaya, T. Matsui, D. Fujita, *Sci. Rep.* **2015**, *5*, 11141.
- [13] X. Shi, H. Jeong, S. J. Oh, M. Ma, K. Zhang, J. Kwon, I. T. Choi, I. Y. Choi, H. K. Kim, J. K. Kim, *Nat. Commun.* **2016**, *7*:11943.
- [14] S. M. Sze, *Physics of Semiconductor Devices*, John Wiley & Sons, New York **1981**.
- [15] A. J. Bosman, H. J. Vandaal, *Adv. Phys.* **1970**, *19*, 1.
- [16] A. J. E. Rettie, H. C. Lee, L. G. Marshall, J. F. Lin, C. Capan, J. Lindemuth, J. S. McCloy, J. Zhou, A. J. Bard, C. B. Mullins, *J. Am. Chem. Soc.* **2013**, *135*, 11389.
- [17] F. F. Abdi, T. J. Savenije, M. M. May, B. Dam, R. van de Krol, *J. Phys. Chem. Lett.* **2013**, *4*, 2752.
- [18] N. J. Cherepy, D. B. Liston, J. A. Lovejoy, H. M. Deng, J. Z. Zhang, *J. Phys. Chem. B* **1998**, *102*, 770.
- [19] A. G. Joly, J. R. Williams, S. A. Chambers, G. Xiong, W. P. Hess, D. M. Laman, *J. Appl. Phys.* **2006**, *99*.
- [20] A. J. Rettie, W. D. Chemelewski, D. Emin, C. B. Mullins, *J. Phys. Chem. Lett.* **2016**, *7*, 471.
- [21] K. E. Kweon, G. S. Hwang, J. Kim, S. Kim, S. Kim, *Phys. Chem. Chem. Phys.* **2015**, *17*, 256.
- [22] D. Emin, *Polarons*, Cambridge University Press, Cambridge **2012**.
- [23] X. Chen, L. Liu, Y. Y. Peter, S. S. Mao, *Science* **2011**, *331*, 746.
- [24] G. Wang, Y. Ling, X. Lu, F. Qian, Y. Tong, J. Z. Zhang, V. Lordi, C. Rocha Leao, Y. Li, *J. Phys. Chem. C* **2013**, *117*, 10957.
- [25] G. Wang, Y. Ling, H. Wang, X. Yang, C. Wang, J. Z. Zhang, Y. Li, *Energy Environ. Sci.* **2012**, *5*, 6180.
- [26] G. Wang, Y. Ling, Y. Li, *Nanoscale* **2012**, *4*, 6682.
- [27] G. Wang, H. Wang, Y. Ling, Y. Tang, X. Yang, R. C. Fitzmorris, C. Wang, J. Z. Zhang, Y. Li, *Nano Lett.* **2011**, *11*, 3026.
- [28] Y. Ling, G. Wang, J. Reddy, C. Wang, J. Z. Zhang, Y. Li, *Angew. Chem. Int. Ed.* **2012**, *51*, 4074.
- [29] J. K. Cooper, S. B. Scott, Y. Ling, J. Yang, S. Hao, Y. Li, F. M. Toma, M. Stutzmann, K. V. Lakshmi, I. D. Sharp, *Chem. Mater.* **2016**, *28*, 5761.
- [30] D. K. Zhong, S. Choi, D. R. Gamelin, *J. Am. Chem. Soc.* **2011**, *133*, 18370.
- [31] C. Schwab, M. Hofmann, R. Heller, J. Seiffe, J. Rentsch, R. Preu, *Phys. Status Solidi (a)* **2013**, *210*, 2399.
- [32] W. Tillmann, F. Hoffmann, S. Momeni, R. Heller, *Surf. Coat. Technol.* **2011**, *206*, 1705.
- [33] T. W. Kim, K.-S. Choi, *Science* **2014**, *343*, 990.
- [34] F. F. Abdi, N. Firet, R. van de Krol, *ChemCatChem* **2013**, *5*, 490.
- [35] H. Dotan, K. Sivula, M. Gratzel, A. Rothschild, S. C. Warren, *Energy Environ. Sci.* **2011**, *4*, 958.
- [36] V. Fidelsky, M. C. Toroker, *J. Phys. Chem. C* **2016**, *120*, 25405.
- [37] O. Diaz-Morales, D. Ferrus-Suspedra, M. T. M. Koper, *Chem. Sci.* **2016**, *7*, 2639.
- [38] J. H. Kim, Y. Jo, J. H. Kim, J. W. Jang, H. J. Kang, Y. H. Lee, D. S. Kim, Y. Jun, J. S. Lee, *ACS Nano* **2015**, *9*, 11820.
- [39] J. E. Kroeze, T. J. Savenije, J. M. Warman, *J. Am. Chem. Soc.* **2004**, *126*, 7608.
- [40] T. J. Savenije, A. J. Ferguson, N. Kopidakis, G. Rumbles, *J. Phys. Chem. C* **2013**, *117*, 24085.
- [41] D. Friedrich, M. Kunst, *J. Phys. Chem. C* **2011**, *115*, 16657.
- [42] A. Marchioro, J. Teuscher, D. Friedrich, M. Kunst, R. van De Krol, T. Moehl, M. Grätzel, J.-E. Moser, *Nat. Photon.* **2014**, *8*, 250.
- [43] Z. Y. Zhao, Z. S. Li, Z. G. Zou, *Phys. Chem. Chem. Phys.* **2011**, *13*, 4746.

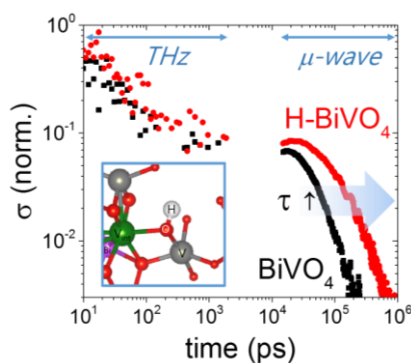
- [44] K. P. S. Parmar, H. J. Kang, A. Bist, P. Dua, J. S. Jang, J. S. Lee, *ChemSusChem* **2012**, *5*, 1926.
- [45] T. J. Savenije, M. P. de Haas, J. M. Warman, *Z. Phys. Chem.* **1999**, *212*, 201.
- [46] T. J. Savenije, A. Huijser, M. J. Vermeulen, R. Katoh, *Chem. Phys. Lett.* **2008**, *461*, 93.
- [47] D. Friedrich, M. Kunst, *Nano Energy* **2012**, *1*, 303.
- [48] J. Reichman, *Appl. Phys. Lett.* **1980**, *36*, 574.
- [49] W. J. Yin, S. H. Wei, M. M. Al-Jassim, J. Turner, Y. Yan, *Phys. Rev. B* **2011**, 83.
- [50] M. Harb, P. Sautet, E. Nurlaela, P. Raybaud, L. Cavallo, K. Domen, J.-M. Basset, K. Takanabe, *Phys. Chem. Chem. Phys.* **2014**, *16*, 20548.
- [51] M. Harb, P. Sautet, P. Raybaud, *J. Phys. Chem. C* **2011**, *115*, 19394.
- [52] M. Harb, P. Sautet, P. Raybaud, *J. Phys. Chem. C* **2013**, *117*, 8892.
- [53] M. Harb, *J. Phys. Chem. C* **2015**, *119*, 4565.
- [54] M. Harb, L. Cavallo, *ACS Omega* **2016**, *1*, 1041.
- [55] H. Zhu, D. C. Rosenfeld, M. Harb, D. H. Anjum, M. N. Hedhili, S. Ould-Chikh, J.-M. Basset, *ACS Catal.* **2016**, *6*, 2852.
- [56] F. A. Kröger, *The chemistry of imperfect crystals*, North-Holland Publishing Co., Amsterdam **1964**.
- [57] M. Ziwrtsch, S. n. Müller, H. Hempel, T. Unold, F. F. Abdi, R. van de Krol, D. Friedrich, R. Eichberger, *ACS Energy Lett.* **2016**, *1*, 888.
- [58] C. Strothkämper, A. Bartelt, P. Sippel, T. Hannappel, R. Schütz, R. Eichberger, *J. Phys. Chem. C* **2013**, *117*, 17901.
- [59] H. Němec, P. Kužel, V. Sundström, *J Photochem. Photobiol. A Chem.* **2010**, *215*, 123.
- [60] R. Ulbricht, E. Hendry, J. Shan, T. F. Heinz, M. Bonn, *Rev. Mod. Phys.* **2011**, *83*, 543.
- [61] L. Avakyants, A. Chervyakov, V. Gorelik, P. Sverbil', *J. Russ. Laser Res.* **2004**, *25*, 535.
- [62] F. F. Abdi, R. van de Krol, *J. Phys. Chem. C* **2012**, *116*, 9398.
- [63] F. F. Abdi, N. Firet, A. Dabirian, R. van de Krol, *MRS Online Proc. Lib.* **2012**, 1446. DOI: 10.1557/opl.2012.811.
- [64] C. Strothkämper, K. Schwarzburg, R. Schütz, R. Eichberger, A. Bartelt, *J. Phys. Chem. C* **2012**, *116*, 1165.
- [65] G. Kresse, J. Hafner, *Phys. Rev. B* **1994**, *49*, 14251.
- [66] G. Kresse, J. Furthmüller, *Phys. Rev. B* **1996**, *54*, 11169.
- [67] G. Kresse, J. Furthmüller, *Comput. Mater. Sci.* **1996**, *6*, 15.
- [68] G. Kresse, D. Joubert, *Phys. Rev. B* **1999**, *59*, 1758.
- [69] J. P. Perdew, K. Burke, M. Ernzerhof, *Phys. Rev. Lett.* **1996**, *77*, 3865.
- [70] P. E. Blöchl, *Phys. Rev. B* **1994**, *50*, 17953.
- [71] H. J. Monkhorst, J. D. Pack, *Phys. Rev. B* **1976**, *13*, 5188.
- [72] B. Delley, *J. Chem. Phys.* **2000**, *113*, 7756.
- [73] B. Delley, *J. Chem. Phys.* **1990**, *92*, 508.
- [74] M. Harb, D. Masih, S. Ould-Chikh, P. Sautet, J.-M. Basset, K. Takanabe, *J. Phys. Chem. C* **2013**, *117*, 17477.
- [75] M. Harb, D. Masih, K. Takanabe, *Phys. Chem. Chem. Phys.* **2014**, *16*, 18198.
- [76] M. Harb, A. Ziani, K. Takanabe, *Phys. Status Solidi (b)* **2016**, *253*, 1115.
- [77] S. Lardhi, A. Curutchet, L. Cavallo, M. Harb, T. Le Bahers, *Phys. Chem. Chem. Phys.* **2017**, *19*, 12321.
- [78] S. Lardhi, D. Noureldine, M. Harb, A. Ziani, L. Cavallo, K. Takanabe, *J. Chem. Phys.* **2016**, *144*, 134702.
- [79] D. Noureldine, S. Lardhi, A. Ziani, M. Harb, L. Cavallo, K. Takanabe, *J. Mater. Chem. C* **2015**, *3*, 12032.
- [80] J. Paier, M. Marsman, K. Hummer, G. Kresse, I. C. Gerber, J. G. Ángyán, *J. Chem. Phys.* **2006**, *124*, 154709.
- [81] A. Zhang, J. Zhang, *Mater. Sci-Poland* **2009**, *27*, 1015.

Overcoming poor charge carrier transport represents one of the biggest challenges in the development of metal oxide photoelectrodes. Time-resolved conductivity measurements and DFT calculations reveal that a simple post-synthesis hydrogen treatment at 300 °C reduced the number of deep trap states in metal oxides. As a result, the charge carrier lifetime and overall photoelectrochemical performance are significantly enhanced.

Keyword: solar water splitting, BiVO_4 , time-resolved spectroscopy, hydrogen treatment, carrier lifetime

*Ji-Wook Jang, Dennis Friedrich, Sönke Müller, Marlene Lamers, Hannes Hempel, Sheikha Lardhi, Zhen Cao, Moussab Harb, Luigi Cavallo, René Heller, Rainer Eichberger, Roel van de Krol, and Fatwa F. Abdi**

Enhancing charge carrier lifetime in metal oxide photoelectrodes through mild hydrogen treatment



Supporting Information

Enhancing charge carrier lifetime in metal oxide photoelectrodes through mild hydrogen treatment

*Ji-Wook Jang, Dennis Friedrich, Sönke Müller, Marlene Lamers, Hannes Hempel, Sheikha Lardhi, Zhen Cao, Moussab Harb, Luigi Cavallo, René Heller, Rainer Eichberger, Roel van de Krol, and Fatwa F. Abdi**

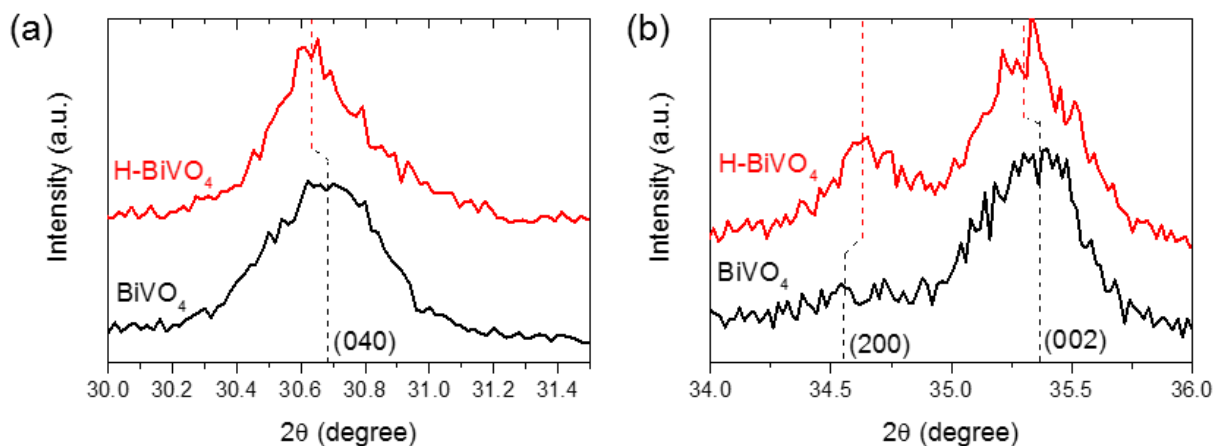


Figure S1. Observed shifts in the (a) (040) and (b) (200) and (002) x-ray diffraction peaks with hydrogen treatment.

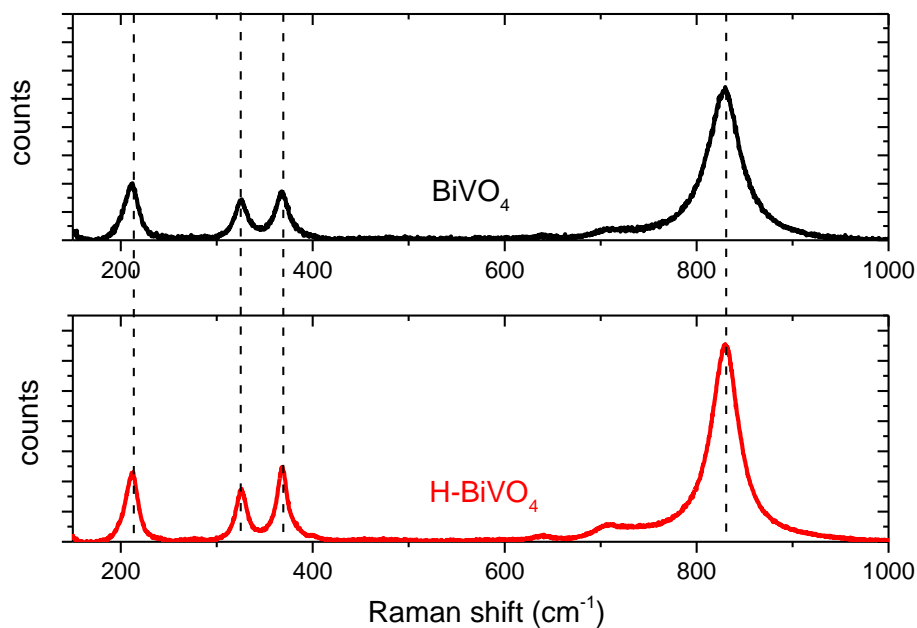


Figure S2. Raman spectra of pristine and hydrogen-treated BiVO_4 . Peaks at ~ 830 , 368, 326 and 212 cm^{-1} are assigned to ν_s (V-O), δ_s (VO_4^{3-}), δ_{as} (VO_4^{3-}) and external modes, respectively.^[81]

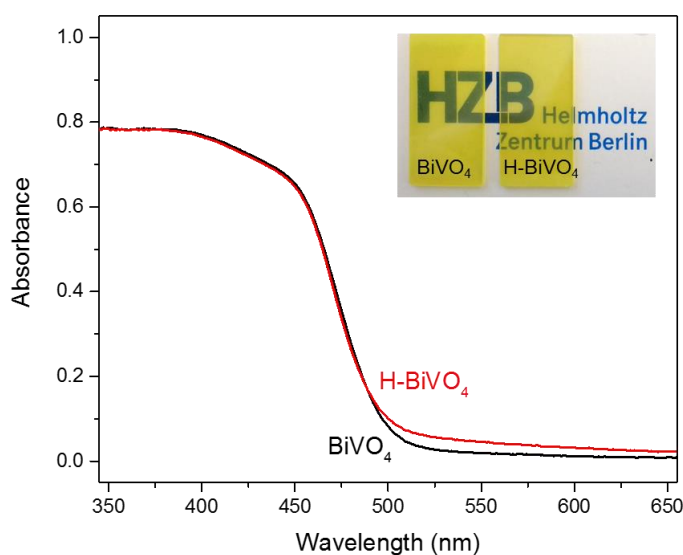


Figure S3. Absorbance spectra of pristine and hydrogen-treated BiVO_4 films measured with UV-Vis spectroscopy. The inset shows the photograph of both films deposited on quartz.

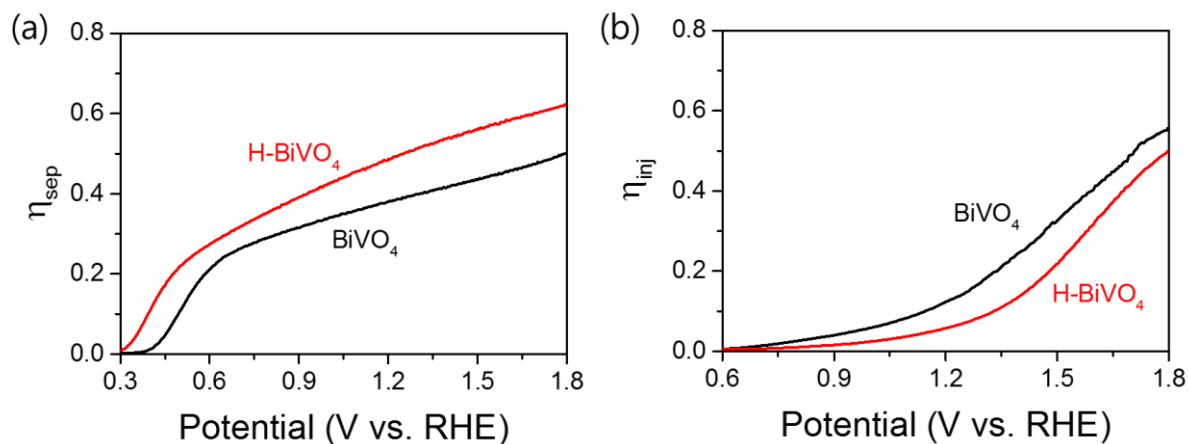


Figure S4. (a) Carrier separation efficiency (η_{sep}) and (b) carrier injection efficiency (η_{inj}) of pristine and hydrogen-treated BiVO₄ as a function of applied potential.

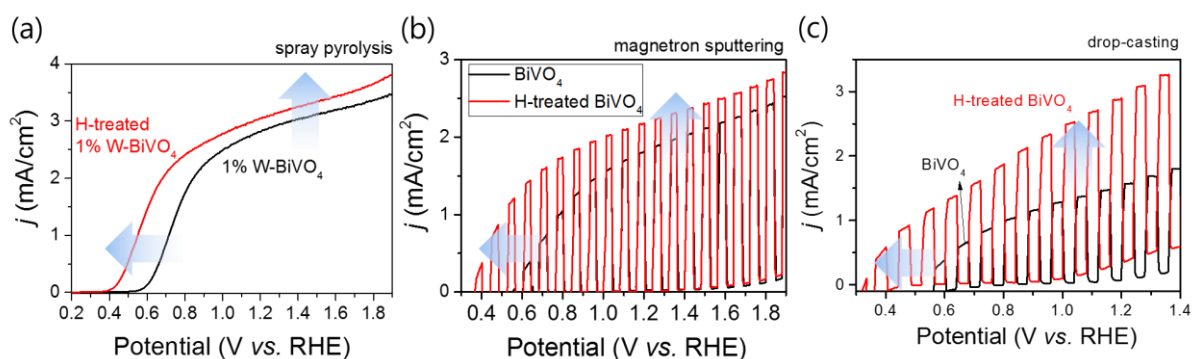


Figure S5. The effect of hydrogen treatment to the photocurrent-voltage (j -V) curve of BiVO₄ is found to be general. The same increase of photocurrent plateau and cathodic shift of onset potential were shown in (a) W-doped BiVO₄ prepared by spray pyrolysis, (b) undoped BiVO₄ prepared by magnetron sputtering, and (c) undoped BiVO₄ made by drop-casting.

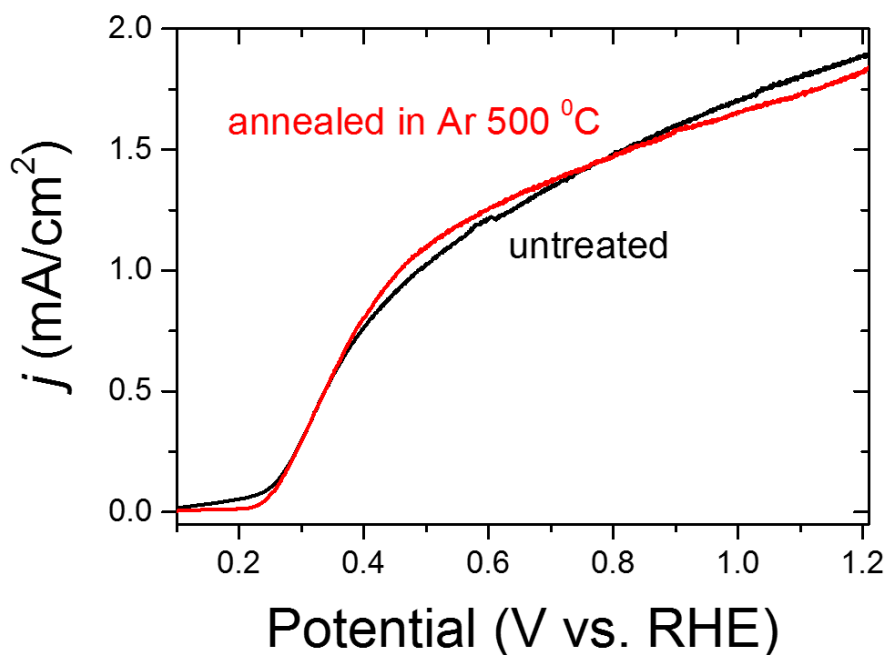


Figure S6. AM1.5 photocurrent-voltage (j - V) curves of untreated 100 nm-thick BiVO_4 and one that is annealed in Ar at 500 °C to increase the oxygen vacancies. The electrolyte is 0.1 M phosphate buffer (KPi, pH \sim 7) and 0.5 M sodium sulphite (Na_2SO_3) as hole scavenger.

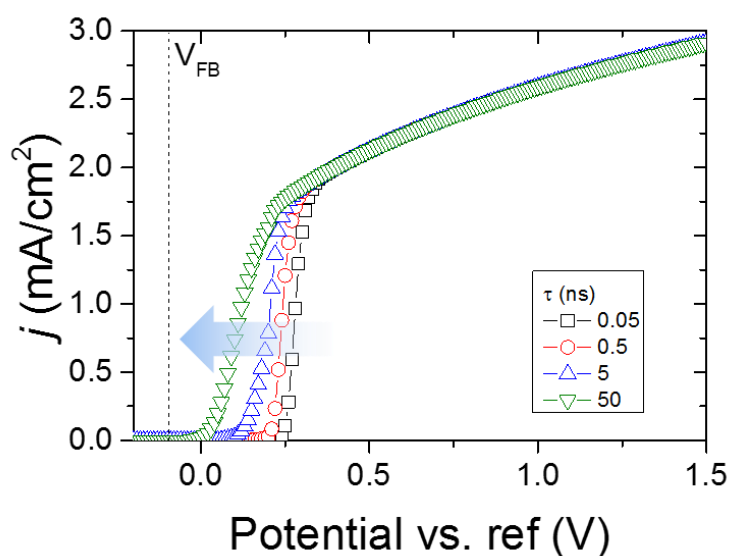


Figure S7. Simulated photocurrent-voltage curve of a hypothetical photoelectrode, illustrating the influence of carrier lifetime to the onset potential. The following parameters were used as the input to the Reichman model^[47]: $I_0 = 10^{20} \text{ photons}\cdot\text{s}^{-1}\cdot\text{m}^{-2}$, $\alpha = 10^6 \text{ m}^{-1}$, $L_D = 100 \text{ nm}$, $N_D = 10^{17} \text{ cm}^{-3}$, I_p^0 (hole exchange current) = $10^{-10} \text{ mA}\cdot\text{cm}^{-2}$.

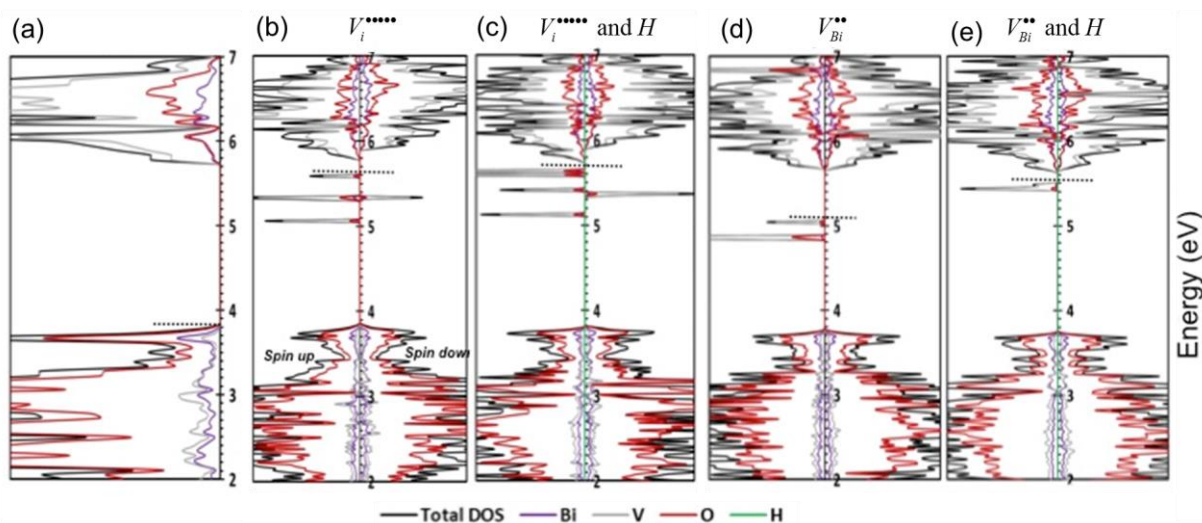


Figure S8. Computed density of states—DOS (based on PBE functional) for (a) pristine BiVO_4 , (b) BiVO_4 with vanadium interstitial before and (c) after hydrogen treatment, and (d) BiVO_4 with vanadium anti-site on bismuth before and (e) after hydrogen treatment. Fermi levels are indicated by the dashed lines.

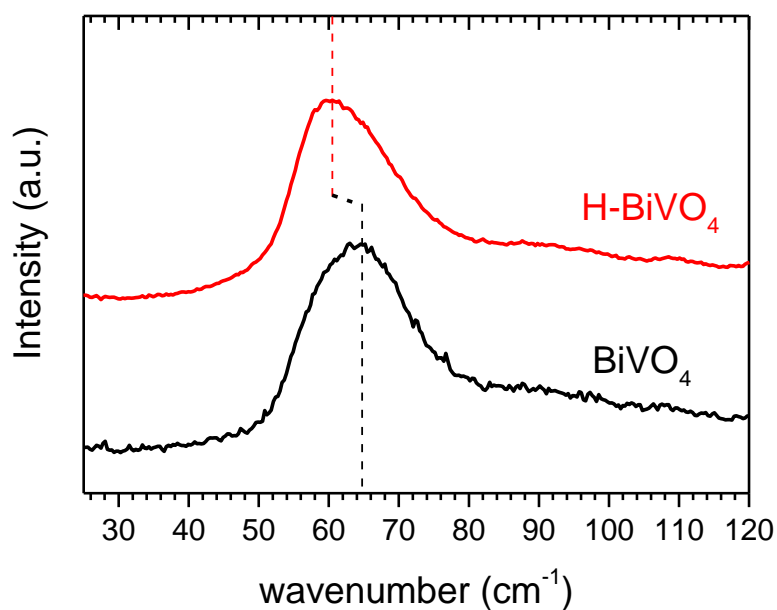


Figure S9. A shift of $\sim 3 \text{ cm}^{-1}$ is observed on the phonon mode corresponding to the external $\text{Bi}^{3+}\text{-VO}_4^{3-}$ vibration upon hydrogen treatment.

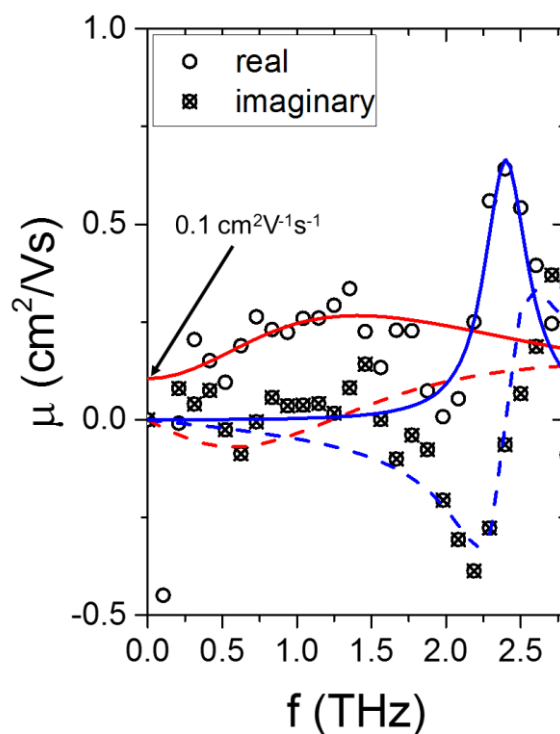


Figure S10. THz combined electron-hole mobility spectra of hydrogen-treated BiVO₄ measured at delay time of 20 ps. The open squares represent the real data points and stars the imaginary data points. Fit was performed according to the procedure reported in our previous report.^[57] The red solid and dashed lines are fit based on Drude-Smith model to the real and imaginary data, respectively. The blue solid and dashed lines are fit based on damped harmonic oscillator model to the real and imaginary data, respectively.

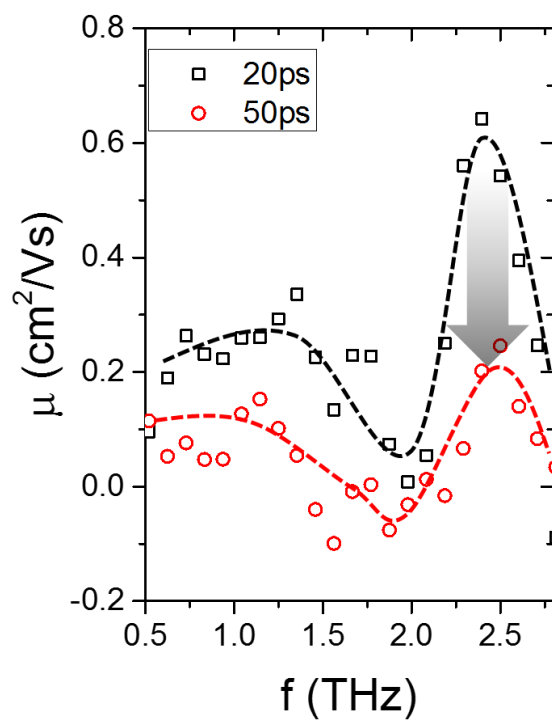


Figure S11. THz combined electron-hole mobility spectra of hydrogen-treated BiVO₄ measured at delay time of 20 and 50 ps. Only the real data are shown.

Table S1. Calculated formation energies for the various explored defective structures before and after hydrogenation, both at temperature of 0 K.

Point defects	Formation energy in BiVO ₄ (eV)	Formation energy in H-BiVO ₄ (eV)
$V_{Bi}^{///}$	0.467	0.347
$V_V^{////}$	0.967	0.765
$V_O^{\bullet\bullet}$	0.319	0.294
$Bi_i^{\bullet\bullet\bullet}$	0.394	0.374
$V_i^{\bullet\bullet\bullet\bullet}$	0.041	0.056
$O_i^{//}$	0.160	0.121
$Bi_V^{//}$	0.446	0.385
$V_{Bi}^{\bullet\bullet}$	0.024	0.052

Table S2. Calculated lattice parameters of the two most stable defect-containing BiVO₄ before and after hydrogenation along with their chemical bonds around the defect site.

Structure	Lattice parameters						Chemical Bonds			
	<i>a</i> (Å)	<i>b</i> (Å)	<i>c</i> (Å)	α (°)	β (°)	γ (°)	V _{int} -O (Å)	V _{int} -V (Å)	V _{int} -Bi (Å)	O-H (Å)
V _i ^{•••••} - containing BiVO ₄	7.27	11.54	5.12	90	134.90	89.90	1.95 1.95 2.04 2.04 2.09 2.09	2.39 2.74 2.74	3.0 3.0	-
V _i ^{•••••} - containing BiVO ₄ (H- treated)	7.30	11.53	5.14	89.84	135.04	90.25	1.94 1.94 2.00 2.08 2.05 2.11	2.4 2.75 3.04	3.0 3.0	0.98
V _{Bi} ^{••} - containing BiVO ₄	7.20	11.53	5.08	90	134.97	90	2.01 2.01 2.02 2.01	-	-	-
V _{Bi} ^{••} - containing BiVO ₄ (H- treated)	7.22	11.55	5.08	89.95	135.04	90.01	1.99 2.00 2.05 2.07	-	-	1.01

Supporting Note: Carrier concentration determination

For the resistivity measurement, BiVO₄ is coated on quartz by spray pyrolysis, followed by electron beam evaporation of gold (Au) using a mask to create well defined contacts (Figure S12). The thickness of BiVO₄ here is ~200 nm and the distance between each Au (*l*) is varied between 0.18 and 0.94 mm. The resistance (*R*) is then measured between two Au contacts using AMETEK Modulab XM Materials Test System under ac configuration (frequency 1 MHz, ac amplitude 10 mV, dc bias 1 V). The resistance as a function of distance was then linearly fitted, and the intercept at the y-axis is taken as the total contact resistance (*R_c*). The resistivity (ρ) and conductivity (σ) of the films were then obtained using the following equations:

$$\rho = (R - R_c) \frac{d}{l} \quad (\text{S1})$$

$$\sigma = \frac{1}{\rho} \quad (\text{S2})$$

d is the thickness of BiVO₄ (200 nm) and *l* is the distance between Au contacts. We also estimated the carrier density (*N_d*) based on σ and μ obtained in TRMC measurement using the following equation:

$$\sigma = e\mu N_d \quad (\text{S3})$$

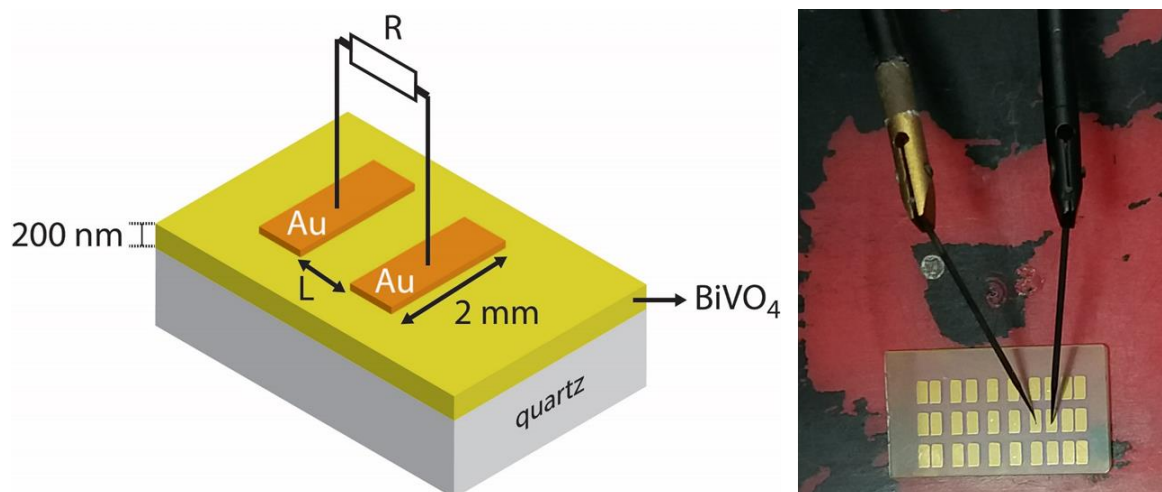


Figure S12. Schematic illustration (left) and photograph (right) depicting the direct resistivity measurement performed on BiVO₄ thin film deposited on quartz.

The resistance as a function of Au contact distance for the hydrogen-treated and tungsten-doped BiVO₄ is shown in Figure S13a. The resistance values obtained from the ac measurement are also compared to the resistance obtained from dc measurement. Both hydrogen-treated and tungsten-doped BiVO₄ show Ohmic behavior, as shown in Figure S13b. The slope of these curves are plotted as the resistances in Fig. S13a, and they are very much in agreement with the ac-acquired data. Based on equations S1-S3, the carrier density values for hydrogen-treated and tungsten-doped BiVO₄ are shown in Table S3 (and Table 2 of the manuscript).

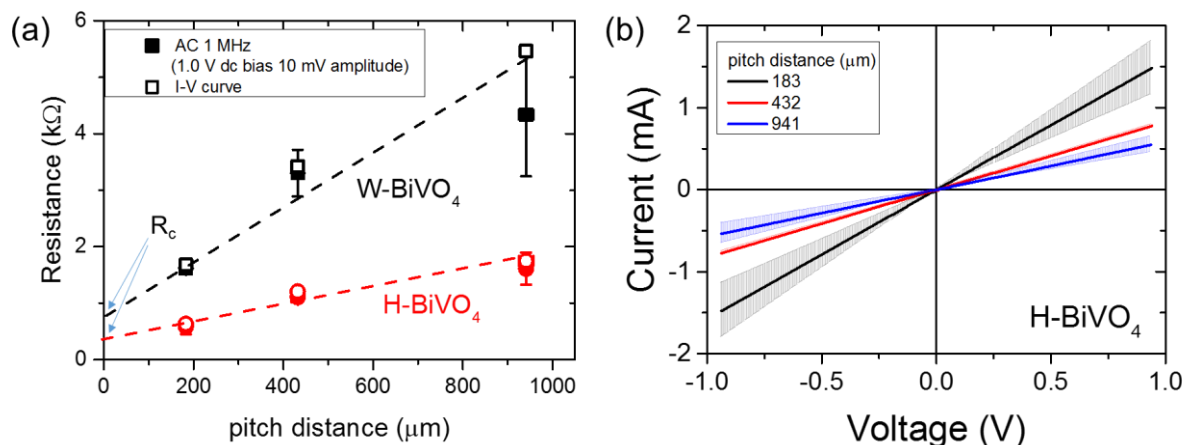


Figure S13. (a) Resistance as a function of pitch distance (i.e., distance between Au contacts in Figure S12) for hydrogen-treated and tungsten-doped BiVO₄. The dashed lines are linear fit to the data and the intercepts to the y-axis represent the contact resistances (R_c) (b) Two-point current-voltage curve of hydrogen-treated BiVO₄ measured with the configuration shown in Figure S12 for different pitch distances. Ohmic behavior is clearly shown.

Table S3. Carrier concentration (N_d) values for pristine, hydrogen-treated and tungsten-doped BiVO₄ measured via two-electrode conductivity, dark microwave conductivity and Mott-Schottky measurements, as described in this section. Two-electrode conductivity measurement on pristine BiVO₄ was not possible due to high contact resistance and Mott-Schottky measurements on hydrogen-treated and tungsten-doped BiVO₄ were not reliable because the requirements were not met.

Photoelectrode	Two-electrode conductivity			Dark μ -wave conductivity	Mott-Schottky
	ρ ($\text{m}\Omega\cdot\text{m}$)	σ (10^3 S m^{-1})	N_d (cm^{-3})	N_d (cm^{-3})	N_d (cm^{-3})
Pristine BiVO ₄	-	-	-	8.7×10^{18}	5.2×10^{18}
H-BiVO ₄	0.8 ± 0.3	1.40 ± 0.4	$1.1 \pm 0.3 \times 10^{21}$	2.4×10^{20}	-
W-BiVO ₄	2.4 ± 0.7	0.45 ± 0.1	$1.4 \pm 0.4 \times 10^{21}$	3.8×10^{21}	-

The method described above, however, were unable to be implemented on the pristine BiVO₄. This is most probably caused by the presence of extremely high contact resistance. Therefore, in order to estimate the carrier concentration of pristine BiVO₄, we utilized dark microwave conductivity measurements. The same setup as the TRMC measurement was used, except no laser pulse illumination was subjected to the films. By comparing the normalized change in the detected dark reflected microwave power from the cavity filled with quartz substrate and thin BiVO₄ layer on quartz, and assuming the small perturbation condition is maintained, we can calculate the change in conductance (i.e., the conductance of BiVO₄) according to the following relationship:

$$\frac{P_{\text{BiVO}_4/\text{quartz}} - P_{\text{quartz}}}{P} = \frac{\Delta P}{P} = -K\Delta G \quad (\text{S4})$$

K is the sensitivity factor derived from the resonance characteristics of the cavity and the dielectric properties of BiVO₄ (a value of 68 was taken here). $\Delta P/P$ values for pristine, hydrogen-treated and tungsten-doped BiVO₄ are 0.003, 0.09, and 0.29, respectively. The conductivity and the carrier concentration can then be calculated according to the following equations:

$$\Delta G = \Delta\sigma\beta d \quad (\text{S5})$$

$$\Delta\sigma = eN_d\mu_e \quad (\text{S6})$$

Here, β is the ratio between the inner broad and narrow dimensions of the waveguide, e is the elementary charge, and d is the thickness of the film. μ_e (Table 1) was taken to calculate the carrier concentration since only majority carriers are considered in the absence of illumination. A value of $8.7 \times 10^{18} \text{ cm}^{-3}$ was obtained for pristine BiVO₄, as shown in Table S3. The values for hydrogen-treated and tungsten-doped BiVO₄ are also shown, which are in the same order of magnitude as compared to the values obtained by the electrical conductivity method.

Finally, to provide further confidence on the estimation of the carrier concentration, we performed a Mott-Schottky measurement on the pristine BiVO₄. Mott-Schottky measurement

assumes that the overall response of the system is dominated by the capacitance of the space charge layer. As shown in the Bode plot of the pristine BiVO₄ (Figure S14a) this is the case for frequencies around 1 kHz: the real part of the impedance is constant, and the imaginary part has a slope close to -1 when plotted against frequency on a log-log scale.

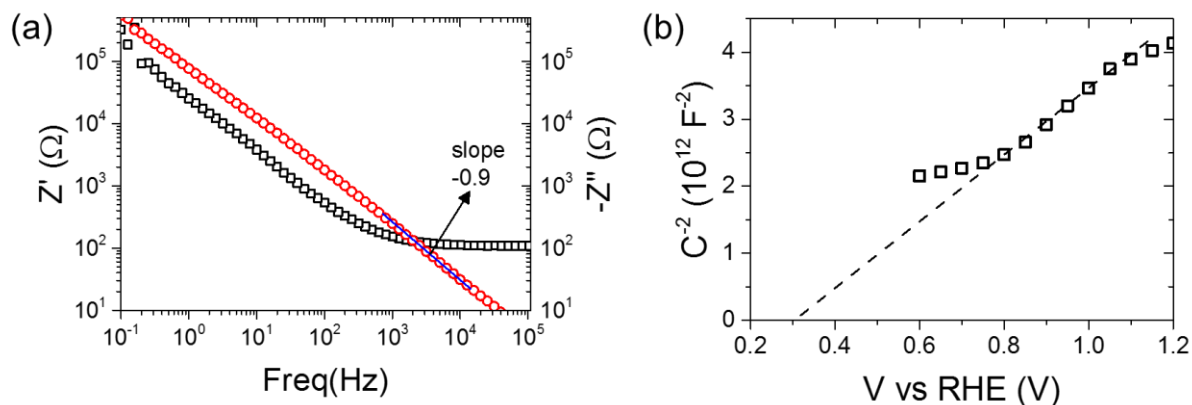


Figure S14. (a) Log-log plot of real (Z') and imaginary (Z'') impedance as a function of frequency of potential modulation of the pristine BiVO₄ film, at applied potential of 0.8 V vs RHE. (b) Mott-Schottky plot for the pristine BiVO₄ film, measured at 1 kHz. The electrolyte used in the measurement is 0.1 M KPi with 0.5 M Na₂SO₃.

A Mott-Schottky plot of pristine BiVO₄ is shown in Figure S14b, measured at 1 kHz. For the linear part of the slope, the following equation applies:

$$\frac{1}{C^2} = \frac{2}{eN_d \epsilon_0 \epsilon_r A^2} \left(V_{appl} - V_{FB} - \frac{kT}{e} \right)$$

From the slope of Figure S14b, a donor density value of $5.2 \times 10^{18} \text{ cm}^{-3}$ was obtained, which is very close to the value obtained from the dark microwave conductivity measurement.

The Mott-Schottky condition was, however, not met at all frequencies for the hydrogen-treated and tungsten-doped BiVO₄, preventing reliable Mott-Schottky analysis. Nevertheless, Table S3 provides carrier concentration values that are comparable between different

measurement techniques, which provide confidence that the conclusion taken here is valid:
hydrogen treatment increases the carrier concentration in BiVO_4 .